RESEARCH: Review

Perspectives on solution processing of two-dimensional MXenes

Sina Abdolhosseinzadeh [1,2], Xiantao Jiang [3,4], Han Zhang [4], Jieshan Qiu [5], Chuanfang (John) Zhang [1,*]

[1] Laboratory for Functional Polymers, Empa, Swiss Federal Laboratories for Materials Science and Technology, Überlandstrasse 129, CH-8600 Dübendorf, Switzerland
[2] Institute of Materials Science and Engineering, Ecole Polytechnique Fedérale de Lausanne (EPFL), Station 12, CH-1015 Lausanne, Switzerland
[3] College of Chemistry and Environmental Engineering, Shenzhen University, Shenzhen 518060, China
[4] Shenzhen Engineering Laboratory of Phosphorene and Optoelectronics, Collaborative Innovation Center for Optoelectronic Science and Technology, College of Optoelectronic Engineering, Shenzhen University, Shenzhen 518060, China
[5] College of Chemical Engineering, Beijing University of Chemical Technology, Beijing 100029, China

Since the discovery of two-dimensional (2D) transition metal carbides and nitrides, known as MXenes, research on these wonder 2D inorganic compounds has become increasingly intensified with their members quickly expanding. MXenes' state-of-the-art applications are heavily dependent on their processing strategies and manufacturing methods. Nevertheless, the solution processing of MXenes has not been comprehensively reviewed. This review summarizes progress regarding solution processing of MXenes over the past decade as well as outlines key perspectives for future scalable manufacturing strategies. Etching of MAX phases and delamination of MXene are briefly introduced. Rheological properties of MXene dispersions and wetting of the MXene inks, which are crucial for the achievement of high-resolution printing and homogeneous coating, are discussed in detail. We have discussed the ink formulation strategies and fine-tuning of the ink properties to match with that of the targeted substrates to yield efficient yet high-quality printed/coated films/structures. As such, we demonstrate a "map of guidelines" for solution-based processing of MXenes toward high-performance applications, such as electrochemical energy storage, conductive electrodes, electromagnetic interference shielding, and so on.

Introduction

The exotic properties of graphene, mechanically exfoliated from graphite, indicated that by thinning down the thickness of three-dimensional materials to 2D atomically thin sheets, electrical, optical, mechanical, and electrochemical properties can be adjusted profoundly [1–6]. This groundbreaking discovery greatly proliferated the studies on the synthesis and characterizations of high-quality 2D materials beyond graphene [7–10]. Transition metal dichalcogenides (TMDs) and oxides (TMOs) [11–15], silicene [16], germanene [17], borophene [18], etc., are all fascinating 2D materials, adding a large diversity with unique properties to this 2D family, which is still expanding quickly.

Transition metal carbides, carbonitrides, and nitrides, known as MXenes, are a new class of 2D materials that have attracted an ever-increasing research attention in many aspects, and are standing at the frontier of the 2D materials community [17,19]. Up to now, over 30 MXene members have been experimentally synthesized and many more (hundreds) are predicted to be thermodynamically stable [20]. Therefore, unlike other 2D materials, MXenes themselves are a big family of materials with a diversity of properties such as high electrical conductivity, volumetric capacitance, and electromagnetic interference shielding performance [19,21–24]. These outstanding performances suggest that

* Corresponding author.
E-mail address: Zhang, C.J. (chuanfang.zhang@empa.ch)

MXenes are promising in many applications such as electrochemical energy storage, transparent conductive electrodes and electrical contacts for thin-film transistors, electromagnetic interference shielding, photodetectors, sensing, etc. [19,25–33]. Central to these applications lies in the fabrication of advanced MXene-based architectures, including nanostructured electrodes, high-quality continuous thin films/contacts, as well as patterns toward functional devices.

Amongst different processing methods, solution processing is arguably the most widely used technique as it enables the scalable production of high quality MXene films/structures. The solution-based methods are also highly preferred since MXenes are mainly synthesized in solutions (will be discussed later). Understanding the basic principles of individual processing routes, and matching the physicochemical properties of MXenes (such as rheology, particle size, terminal groups, etc.) with the surface chemistry of target substrates, are of paramount importance for efficient manufacturing of MXene-based functional devices. For instance, inkjet printing, which allows the formation of high-resolution paths on a small footprint area, requires inks with low solid content and specific rheological properties; too viscous inks are not jettable, and large particle sizes inevitably lead to nozzle clogging issues [34,35]. On the other hand, screen printing and extrusion printing require high solid content with specific yield strength and pseudoplasticity [36]. Therefore, MXene properties such as morphology, rheology, concentration, etc., heavily determine the corresponding processing strategies that are the most efficient at the lowest manufacturing cost. In other words, outlining a "property-process map" for guiding MXene processing is of significance to bridge the MXene materials and functional devices. Although numerous excellent reviews are available on the synthesis, properties, and applications of MXenes [37–39], little attention has been paid to their solution processing and its fundamentals.

For an easy integration, aimed at MXene beginners, milestones of etching routes and delamination strategies, as well as the important physicochemical properties of the MXenes are briefly reviewed in the second section. Advanced readers may skip this section and continue reading from the third section where we have first discussed the basics of solution processing, and then, the colloidal and rheological properties of MXenes. In the fourth and the fifth sections, we have reviewed the recent developments in the MXenes solution processing, including printing (inkjet-, extrusion-, screen-, etc.) and coating (blade-, spin-, spray-, etc.), and provided guidelines for ink formulation and application of each method. Finally, challenges on MXenes processing toward high-performance thin films/devices and future perspectives are provided and explained in the last section.

Synthesis of MXenes and their properties

MXenes have the general formula of $M_{n+1}X_n$, where M is a transition metal (such as Ti, Sc, Nb, V, Mo, Zr, Hf, Cr, etc.) and X is carbon and/or nitrogen. A single layer of MXene is composed of n layers of element X alternatively sandwiched between $n + 1$ layers of element M [40]. MXenes are typically obtained by the selective removal of "A" atomic layers from MAX phases, where A is an element from group 13 or 14 in the periodic table such as Al or Ga (M and X refer to the same elements in MXenes) [9,40–44]. Due to the strong chemical bonds of M–A–M, mechanical cleavage of the MAX precursors is challenging and has low yields [45], as a result, chemical etching methods were developed. The first reported MXene ($Ti_3C_2T_x$), was obtained by the selective etching of Al layers from Ti_3AlC_2 in a concentrated hydrofluoric acid (HF) solution [44]. Following this groundbreaking discovery, dozens of other MXenes were also successfully prepared by the HF-etching method. When MXenes are synthesized by wet-etching processes, their surfaces are terminated by functional groups and their general formula is written as $M_{n+1}X_nT_x$ where T_x represents the functional groups. Flake size, surface chemistry, and defects density of the delaminated flakes are etching routes-dependent; changing from HF etching to non-HF etching inevitably results in MXenes with different physicochemical properties [46], which further influence their processability. Thus, before discussing the solution processing of MXenes, we summarize their synthesis routes (etching and delamination) as well as their physicochemical properties in brief.

Etching and delamination of MXenes

MXene selective etching routes

To prepare monolayer or few-layer MXenes, the first step is the selective etching of MAX phases. These routes include HF etching, fluoride-containing etching, alkali etching, and molten-salts etching. Fig. 1a shows the major milestones regarding selective etching to give multilayered MXenes. As the first developed method, HF etching is efficient in etching the MAX phases and gives corresponding MXenes with accordion-like structure [40,44]. In a typical run, 1 g of Ti_3AlC_2 is slowly added to 10 mL of a 50 wt.% concentrated HF solution and stirred for 2 h at room temperature, where the following reactions occur [9,44]:

$$Ti_3AlC_2(s)+3HF(aq)=Ti_3C_2(s)+AlF_3(aq)+1.5H_2(g) \quad (1)$$

$$Ti_3C_2(s)+2HF(aq)=Ti_3C_2F_2(s)+H_2(g) \quad (2)$$

$$Ti_3C_2(s)+2H_2O(aq)=Ti_3C_2(OH)_2(s)+H_2(g) \quad (3)$$

The proof of a successful etching trial should be based on X-ray diffraction (XRD) patterns rather than scanning electron microscopy (SEM) images, as the etched multilayered MXene may not necessarily showcases an accordion-like morphology [47]. The absence of characteristic peaks of Ti_3AlC_2 MAX phase coupled with a strong peak centering at 9.5°, which is attributed to the (0 0 2) plane of $Ti_3C_2T_x$ MXene, is a generally accepted criterion for the successfulness of a synthesis [47]. It is worth mentioning that the etching conditions are MAX-phase-dependent. For instance, Nb_2AlC MAX phase requires 90 h of etching in a 50 wt.% HF solution [48], while a Ti_3AlC_2 MAX phase only needs 24 h of immersion in a 5 wt.% HF solution [47]. In general, a higher value of n in the MAX phase requires more concentrated HF and/or longer etching time (e.g. $Nb_4C_3T_x$ needs two times longer etching than Nb_2CT_x under similar etching conditions) [49].

Different HF concentrations leads to a variety of surface functionalities (-OH, -O and/or -F) as well as different density of defects. Etching in less-concentrated HF solutions results in more

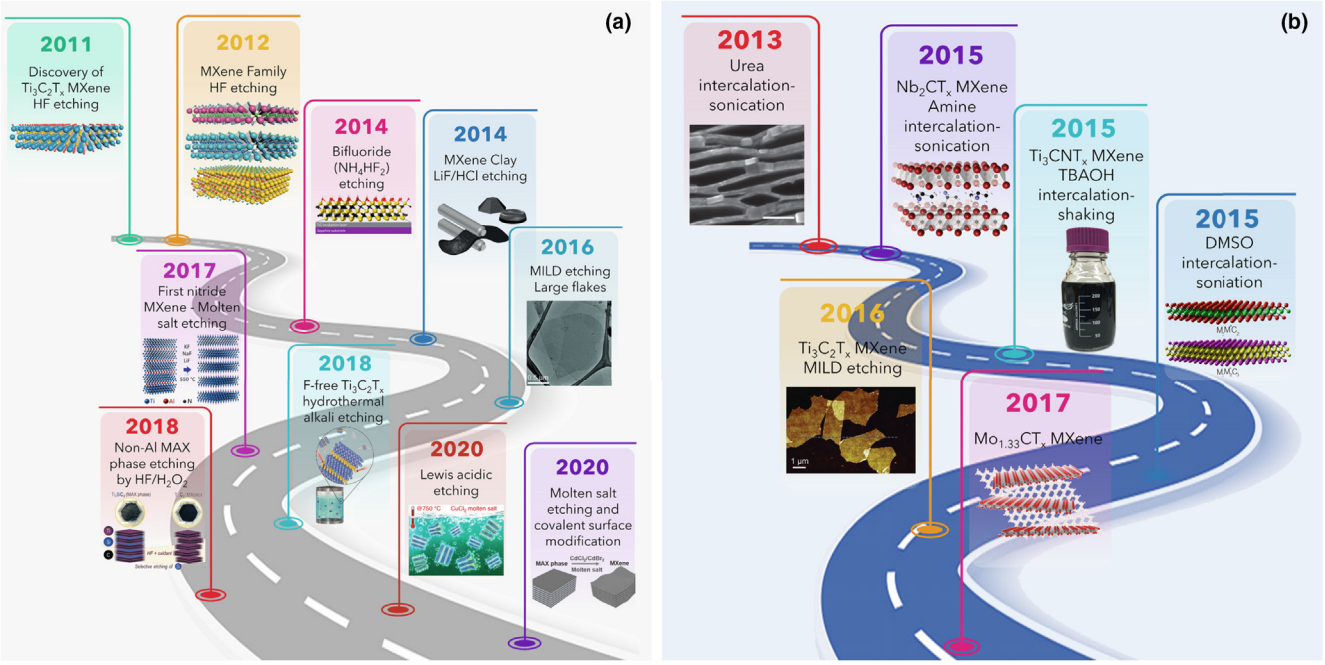

FIGURE 1

Milestones of etching MAX phases and delamination of multilayered MXenes. (a) The first MXene member, $Ti_3C_2T_x$, was firstly reported in 2011 and other members discovered in 2012, using HF etching route. In 2014, $Ti_3C_2T_x$ was etched by ammonium bifluoride (reproduced from ref. [57] with permission from American Chemical Society) and by LiF + HCl (reproduced from ref. [54] with permission from Springer Nature) routes, respectively. A modified route of LiF + HCl was reported using excessive LiF to give high-quality MXene flakes (reproduced from ref. [46] with permission from Wiley-VCH). The first nitride MXene, $Ti_4N_3T_x$, was reported in 2017 using fluoride molten salt etching (reproduced from ref. [63] with permission from Royal Society of Chemistry), while the F-free MXene was obtained through hydrothermal alkali etching (reproduced from ref. [59] with permission from Wiley-VCH). In addition, $Ti_3C_2T_x$ MXene from non-Al MAX (Ti_3SiC_2) was reported in 2018 using HF-H_2O_2 as etchant (reproduced from ref. [62] with permission from Wiley-VCH). In 2020, MXenes were reported using Lewis acidic etching with tunable terminated surface chemistry (reproduced from ref. [22,66] with permission from Springer Nature and AAAS, respectively). (b) MXenes were firstly delaminated using urea intercalation assisted by sonication in 2013 (reproduced from ref. [43] with permission from Springer Nature), then amine was found to be effective in swelling the Nb_2CT_x (reproduced from ref. [67] with permission from Wiley-VCH). In 2015, Ti_3CNT_x was intercalated by TBAOH followed by manual shaking (reproduced from ref. [68] with permission from Royal Society of Chemistry) while double-metal MXenes were firstly reported through DMSO intercalation (reproduced from ref. [51] with permission from American Chemical Society). In 2016, large-size MXene was produced through increasing lithium salt amount such that Li^+ pre-intercalate into MXenes, allowing the ease delamination through manual shaking (reproduced from ref. [46] with permission from Wiley-VCH). In 2017, MXenes with in-plane ordered vacancies was firstly produced (reproduced from ref. [52] with permission from Springer Nature).

O and less F (higher O/F ratio) terminated on the MXene surface, while etching in a more-concentrated HF solution leads to MXenes with more defects/pin-holes and stronger interlayer interactions [46,50]. This allows the effective tuning of the surface chemistry and properties of the MXenes. After etching, the metallic M–A bonds are replaced by weak bonds such as hydrogen and van der Waals bonds, providing vast possibilities for intercalation chemistry while ensuring the delamination into monolayer or few-layer flakes, as will be discussed below.

Besides mono-metal $M_{n+1}AX_n$, double-metal MXenes can also be produced through concentrated HF etching of the corresponding $M'_2M''AlC_2$ and $M'_2M''_2AlC_3$ phases, where M′ (outer layer metal) and M″ (inner layer metal) are Ti, V, Nb, Ta, Cr or Mo with M′ and M″ located in different planes (*out-of-plane* ordering MAX phases, *o*-MAX) [51]. Double-metal MXenes, including $Mo_2TiC_2T_x$, $Mo_2Ti_2C_3T_x$, and $Cr_2TiC_2T_x$, were reported in 2015 through etching their corresponding MAX phases where A = Al in 48–51% HF solution for different durations [51]. In particular, by selectively etching *in-plane* ordering $(M'_{2/3}M''_{1/3})_2AC$ (*i*-MAX phases), *i*-MXenes with *in-plane* ordered vacancies can be prepared through HF route. A typical example is $Mo_{1.33}CT_x$ which is obtained by etching Y (or Sc) and Al out from $(Mo_{2/3}Y_{1/3})_2AlC$ (or $(Mo_{2/3}Sc_{1/3})_2AlC$) [52]. The discovery of *i*-MXenes with ordered vacancies greatly expands the MXene family [53].

Considering the hazardous nature of HF acid, a mild etching strategy based on the in-situ formation of HF upon mixing lithium fluoride (LiF) and hydrochloric acid (HCl) was developed in 2014 (Fig. 1a) [54]. By adding 5 M of LiF powder to 6 M HCl solution, a diluted HF solution with a low concentration of 3–5 wt.% is thus formed according to equation (4):

$$\text{LiF (aq.)}+\text{HCl (aq.)}=\text{HF (aq.)}+\text{LiCl (aq.)} \quad (4)$$

It is worth noting that the LiF-HCl etched multilayered MXenes don't exhibit accordion-like structures. Li^+ ions intercalate into multilayered particles and/or exchanges with surface protons to further enlarge the interlayer spacing, as confirmed by a larger shift of the (0 0 2) peak in the XRD pattern of multilayered MXene [54]. Due to their swollen nature, the etched MXenes behave like a "clay". Increasing the molar ratio of LiF to MAX from 5:1 to 7.5:1, and immersing in 9 M HCl instead of 6 M leads to Li^+-preintercalated multilayered-MXenes, allowing delamination into nanosheets upon solvent exchange at ease

(i.e. washing & manual shaking) [46]. Such a modified etching route is called minimally intensive layer delamination (MILD) developed in 2017 (Fig. 1a). Compared to the HF route, MILD route is able to produce MXenes with fewer pin-holes/defects and a higher O/F ratio [46]. Nanosheets delaminated from MILD method are also typically larger in lateral size, ~3 μm vs hundreds of nm from the HF route. Besides etching MAX phases, non-MAX layered ceramics can also be etched and leave out MXenes. For instance, the HF route and LiF-HCl route are able to leach out Ga from Mo_2Ga_2C, ending up Mo_2CT_x [55]. Furthermore, $Zr_3C_2T_x$ and U_2CT_x MXenes were obtained by the removal of Al_3C_3 layers from $Zr_3Al_3C_5$ and $U_2Al_3C_4$, respectively using the HF etching route [56].

Aside from LiF-HCl, other fluoride-based etchants such as hydrogen bifluoride (NH_4HF_2) are also able to remove the A layers from MAX phases (Fig. 1a). By immersing 0.5 g of Ti_3AlC_2 MAX into 10 mL of 2 M NH_4HF_2 solution at room temperature for 24 h, NH_3 and/or NH_4^+-preintercalated multilayered $Ti_3C_2T_x$ MXene is obtained with much larger interlayer spacing between adjacent layers according to the equations (5) and (6) [47,57,58]:

$$Ti_3AlC_2(s)+3NH_4HF_2(aq)=Ti_3C_2(s) + (NH_4)_3AlF_6(aq)+1.5H_2(g) \quad (5)$$

$$Ti_3C_2(s)+aNH_4HF_2(aq)+bH_2O(aq) = (NH_3)_c(NH_4)_dTi_3C_2(OH)_xF_y(s) \quad (6)$$

Although HF or in-situ HF (also fluoride-containing) etching routes are able to etch away the A elements from MAX phases, the strong corrosive nature of the HF as well as the large amounts of the wasted acid after washing raise serious safety issues and environmental concerns. As an alternative, alkali etching has been reported in 2018 to produce good quality MXenes (Fig. 1a). By a hydrothermal reaction of MAX powders with concentrated sodium hydroxide deaerated solution at 270 °C, followed by multiple washing steps, F-free MXene (terminated with –O and OH) is obtained according to the equation (7) and (8) [59]:

$$Ti_3AlC_2\ (s)+OH^- + 5H_2O(aq)=Ti_3C_2(OH)_2\ (s)+Al(OH)_4^-(aq)+2.5H_2(g) \quad (7)$$

$$Ti_3AlC_2\ (s)+OH^- + 5H_2O(aq) = Ti_3C_2O_2\ (s)+Al(OH)_4^-(aq)+3.5H_2(g) \quad (8)$$

Although all the MAX phases can be theoretically etched, the replacement of the A element from Al to Si in the MAX phase drastically increases the difficulty of etching. This is because the Ti-Si bonds are considerably stronger than the Ti-Al bonds in Ti_3AC_2, rendering the resistance of Ti_3SiC_2 to strong acid and bases, regardless of etchant concentration [60,61]. It is until 2018, that the $Ti_3C_2T_x$ MXene was successfully obtained from a MAX phase with an A-element other than Al (Fig. 1a). Such a process relies on a two-step etching in an aqueous mixture of HF-oxidant (such as H_2O_2, HNO_3, $(NH_4)_2S_2O_8$, $KMnO_4$, $FeCl_3$, etc.): (1) stepwise oxidation of the Si layers of the MAX phae by the oxidant and (2) further dissolution of the Si oxides by HF [62]. Producing MXenes from Ti_3SiC_2 is of particular interest since Ti_3SiC_2 is commercially available and is less expensive compared to Ti_3AlC_2.

While carbide MXenes have been frequently reported, the production of nitride MXenes has proven to be quite challenging. HF or in-situ HF routes are unable to leach out the A elements from nitride MAX phases without dissolving the unstable nitride MXenes [17]. The first nitride MXene, $Ti_4N_3T_x$, was reported in 2017 by etching the Ti_4AlN_3 MAX phase in a mixture of fluoride salts (LiF, NaF, KF) at 550 °C (Fig. 1a) [63]. Interestingly, Ti_2NT_x was reported in KF-HCl route, probably due to a small n in the MAX phase which requires a less strong etchant [64]. Nitride MXenes can also be produced through ammoniation of the corresponding carbide MXenes at high temperatures [65].

Very recently, a general etching route was proposed to prepare MXenes through reacting the MAX phases with A = Al, Zn, Si, Ga, by Lewis acidic molten salts (majorly chlorides) at 750 °C (Fig. 1a) [66]. These molten salts include but not limited to: $CuCl_2$, $NiCl_2$, $FeCl_2$, AgCl, $CdCl_2$, $CoCl_2$, etc. [66]. For instance, to etch the Ti_3SiC_2 MAX phase in $CuCl_2$, the Si atomic layers are firstly oxidized into Si^{4+} by the Lewis acid Cu^{2+}, leading to the formation of Cu metal and $SiCl_4$ gas, the latter expands the sheets and create gaps in the resultant multilayered particles. Excessive $CuCl_2$ further reduces the as-formed Ti_3C_2, leading to Cl-terminated Ti_3C_2 and Cu metal. Further washing the etched products in ammonium persulfate (or another chemical whose potential of redox couple is higher than that of Cu^{2+}/Cu) effectively removes the Cu metal while adding O-containing groups to the surface (resulting in $Ti_3C_2O_xCl_y$) [66]. These molten salts-etched MXenes are hardly obtainable by other methods (i.e. HF or in-situ HF routes), broadening the choices of the MAX phases and the functional groups of the MXenes (by choosing other molten salts with anions like Br^-, I^-, SO_4^{2-}, or NO_3^-, etc).

To step forward, Talapin et al. successfully modified the surface chemistry of molten-salts etched MXenes through reacting Br-terminated MXenes with Li_2Se, Li_2O, and $NaNH_2$, which yielded Ti_3C_2Se, Ti_3C_2O, and $Ti_3C_2(NH)$ MXenes, respectively [22]. In -F and -OH terminated MXenes these surface chemistry modifications are not possible since F-Ti and OH-Ti bonds are stronger (as evidenced by much higher bonding energies and bonds formation enthalpies) than the Cl-Ti and the Br-Ti bonds (in Ti-based MXenes) [22]. Additionally, by reacting the $Ti_3C_2Br_2$ and Ti_2CBr_2 with LiH at 300 °C, they were able to produce bare $Ti_3C_2\square_2$ and $Ti_2C\square_2$, respectively, where □ stands for the vacancy sites [22]. These findings allow unprecedented control over MXene surface chemistry and hence on their structural (e.g. in-plane lattice expansion is observed in Ti_3C_2Te and Ti_2CTe) and electronic properties, enabling new applications (e.g. superconducting fields). In other words, the halide molten salts etching route is not only effective in producing multilayered MXenes terminated with halides, but also guarantees exotic properties by replacing/removing the halide elements with other surface terminations.

Multilayered MXene delamination routes

Isolating monolayers or few-layers from multilayered MXenes is of particular interest for both fundamental studies and practical applications (where few-layers are preferred). The key to MXene successful delamination is to weaken the interactions between adjacent layers. To this end, intercalating big organic molecules

or ions, followed by manual shaking or sonication, are plausible ways to prepare single-layer or few-layer MXenes, ending up with stable, colloidal solutions [43,67]. The first report on MXene delamination employed dimethyl sulfoxide (DMSO), urea, hydrazine, and other molecules causing a big swelling of multilayered MXenes (Fig. 1b) [43]. For instance, the *c*-lattice parameter (*c*-LP) increases from 19.5 Å in the pristine $Ti_3C_2T_x$ to 25.5 Å in hydrazine-intercalated $Ti_3C_2T_x$, and further boosts up to 44.8 Å in DMSO/water co-intercalated $Ti_3C_2T_x$ [43]. The huge expansion on the interlayer spacing greatly weakens the bonding between adjacent layers. Subsequent sonication efficiently delaminates the swollen multilayered particles into single- or few-layered flakes with the lateral size around hundreds of nm. For the delamination of Nb_2CT_x, isopropylamine intercalation assisted by stirring for 18 h is required (Fig. 1b) [67].

Besides these polar solvents, large molecules such as organic bases, tetrabutylammonium hydroxide (TBAOH, $(C_4H_9)_4NOH$), choline hydroxide, and n-butylamine, etc., are also able to interact with multilayered MXenes, leading to a large increase in the interlayer spacing (Fig. 1b) [67–69]. For instance, after mixing with TBAOH for 4 h, the *c*-LP in Ti_3CNT_x and V_2CT_x increases to 39.24 Å and 38.72 Å from 21.39 Å and 19.86 Å, respectively. Slight agitation or mild sonication results in full delamination of large quantities MXene dispersions. On the other hand, due to the MXene negative surface charges, metal cations such as Li^+, Na^+, K^+, Mg^{2+}, NH^{4+}, etc., are able to spontaneously intercalate into multilayered MXenes [70], weakening the van der Waals force among the sheets. This is especially true in the LiF-HCl etched multilayered MXenes. For the "clay" route, with the LiF:Ti_3AlC_2 molar ratio of 5 and HCl concentration of 6 M, the sonication is necessary for the complete delamination of the etched MXenes. However, when the LiF:Ti_3AlC_2 molar ratio is 7.5 and the HCl concentration is 9 M, the excessive intercalated Li^+ ions are exchanged with water molecules upon multiple washing and manual shaking steps, leading to the full delamination when the pH 7 is reached. Due to the elimination of the sonication step, this MILD route allows the production of high-quality, low-defect MXene flakes with lateral dimensions of up to 6 μm (Fig. 1b) [46].

Properties of MXenes

Electrical properties

The most outstanding property of the MXenes is their metallic behavior with a well-fixed electron density near the Fermi level, similar to their precursor MAX phases [71]. The electronic band structure can be adjusted by tuning the MXene composition/surface chemistry (e.g. using different etchants), and controlling the intercalated ions, interlayer spacing, defects, and grain boundaries [72,73]. Aside from controlling the MAX phase etching routes, the surface chemistry of MXenes can also be modified through other methods such as aromatic coupling-diazotization to graft sulfonic groups [74]. Annealing MXenes under vacuum or inert gas flow (e.g. Ar, N_2) can remove the surface terminations and/or water molecules that are trapped between the adjacent MXene layers [50,75], increasing the carrier mobility up to 10 times (substantially higher electrical conductivity). Intercalation of ions (i.e., Li^+, Na^+, K^+) can improve the electrical conductivity by increasing the carrier density in MXenes. Nevertheless, intercalating bulky cations into MXene lamellas may also induce the metallic to semiconductor transition due to the great expansion of the interlayer distances and suppression of the inter-flake electron hopping [73].

MXenes' electrical conductivity is also morphology-dependent. For instance, ultrathin, compact MXene films with highly aligned flakes showcase a very high electrical conductivity up to 15,100 S/cm [21,76]. Grain boundaries can affect the electron hopping behavior as well; smaller flakes correspond to more flake boundaries and thus more inter-particle junctions, resulting in an inferior electrical conductivity in the films. This is best evidenced by the much higher conductance on flakes produced from spin-casting method, which produces more compact films (easer electron hopping). On the other hand, MXene-based aerogels are highly porous, which substantially lower down the electrical conductivity by two orders of magnitude [29,77]. Experimentally, metallic MXene, in particular $Ti_3C_2T_x$ films possess higher electrical conductivity than any other 2D materials, including exfoliated graphene, metal sulfides/hydroxides, etc. [5,20]. It is worth noting that the etching methods also affect the electrical conductivity of MXenes; a stronger etchant means higher defects density in the resultant MXene samples. For instance, HF-etched $Ti_3C_2T_x$ powders showcase moderate electrical conductivities (<1000 S/cm) [47,78].

Work function

The work function of MXenes can be adjusted by surface groups through controlling the Fermi level shift and electronic redistribution [79,80]. Based on the surface dipole modification capabilities, MXenes terminated with pure –O groups possess a larger work function compared to pure –F terminated MXenes, followed by bare MXenes and pure –OH terminated MXenes in sequence. According to this principle, one can achieve quite low work function-MXenes by surface modifications ending up with a major percent of –OH functionalities [80]. The work function of $Ti_3C_2T_x$ MXene can be shifted in the range of 3.9–4.8 eV, depending on the annealing temperature associated with the surface termination moieties [81]. Upon high temperature annealing, surface groups tend to decompose while protons escape from hydroxyl groups forming –O terminations. A kelvin probe detection indicates the work function of $Ti_3C_2T_x$ MXene thin film is ~5.3 eV and decreases to 4.6 eV in the –O terminated $Ti_3C_2T_x$ [75,82], being good electrical contacts for semiconductors. Moreover, $Ti_3C_2T_x$ MXene with a very low work function of 4.37 eV is able to form a good Schottky contact with n-Si by van der Waals forces at room temperature, or Schottky-barrier-free contacts, acts as a transparent electrode, etc., enabling the separation and transport of photoinduced carriers in self-driven photodetectors [83,84].

Optical properties

When delaminating multilayered MXene into few-layers suspended in water, a Tyndall effect is typically observed. By performing UV–Vis spectroscopy of ultrathin films made of delaminated flakes, a transmittance up to 97% can be achieved, corresponding to continuous coverage of single-layer MXene nanosheets (supported on a substrate). This implies that monolayer MXene leads to ~3% loss in transmittance, a value that is

quite similar to graphene (2.3% loss per layer) [26,76]. Considering the thickness of a monolayer MXene, which is four times thicker than graphene (1.5 nm vs 0.34 nm), one can expect that the MXene possesses even higher optical transmittance and better optoelectronic properties to those of graphene. In the UV–Vis spectrum, a broad absorption peak ~ 800 nm is typically observed in $Ti_3C_2T_x$ MXene, which is attributed to the inherent out-of-plane interband transition [85,86].

When reducing the lateral dimension of MXene flakes to quantum size (<3 nm), photoluminescence (PL) phenomenon is observed in MXene dispersion due to due to strong quantum confinement. The light emission properties of MXenes can be used for biomedical imaging and as the gain medium of random lasers, such as white lasers [87,88]. The nonlinear optical response of few-layer $Ti_3C_2T_x$ MXene have been systematically investigated from 800 to 1800 nm by z-scan method, showing the one-photon saturable absorption process dominates the nonlinear absorption at low pulse energy coupled with two or multiple-photon absorption processes as increasing the pulse energy [89]. On the other hand, strong two-photon absorption in gapless MXene monolayers is observed, due to structures of the MXene energy bands near the Fermi level [90]. It is worth mentioning that the saturable absorption behavior in MXenes may inspire advanced ultrafast photonics and optoelectronic devices such as ultrafast lasers [91] and photonic diodes [92]. The metallic conductivity of MXenes enable a platform for photon-electron coupling at the surface, facilitating the excitation of surface plasmons and implicating promising applications in biomedical imaging and sensing [85,93].

Magnetic properties

Compared to the optical and electrical properties, the magnetic properties of MXenes are less investigated. There is a big gap between theoretical predictions and experimental verifications. Most of the predicted magnetic MXenes are based on magnetic transition metal elements (i.e. Cr, V, Mn, Fe, Co and Ni) or their mixtures (forming solid-state solutions) [7,94]. Ti_2C and Ti_2N MXenes were claimed to show a nearly half-metallic ferromagnetism [95], while Mn_2C monolayer shows an antiferromagnetism with a high Neel temperature of 720 K [96]. By surface functionalizing, Mn_2CT_x (T = F, Cl, OH, O and H) monolayer turns to a ferromagnetic state with high Curie temperature (520 K) [97]. Bare MXenes were also reported to be ferromagnets; however, solution-etched MXenes are always terminated with functional groups, thus behave different from the theoretical predictions. The first synthesis of magnetic MXenes was reported by Yoon *et al.*, who found the magnetic susceptibilities ($\chi = 5.7 \sim 52 \times 10^{-6}$) of reduced $Ti_3C_2T_x$ are temperature independent as $T > 10$ K, indicative of Pauli paramagnetic properties [98].

Oxidation stability

Oxidation stability of the MXenes, especially in suspensions is a major concern [105,106]. While the oxidation (or partial oxidation) can be used for some applications (e.g. energy storage [107,108], disposable electronics [109], sensing [110]), it is usually avoided when the electrical conductivity is important. Pinholes and defects, which are formed during the synthesis, accelerate the oxidation of MXenes and shorten their shelf life. Water and dissolved oxygen are playing the main role in the oxidation of MXenes; therefore, storing MXene aqueous dispersion in Ar-filled vials and low temperatures (<5 °C) can considerably prolong their shelf life [105,111]. Freezing the aqueous dispersions under −20 °C is reported to be capable of preserving the MXene flakes up to two years [112]. After oxidation, methane (CH_4) gas may evolve from $Ti_3C_2T_x$ dispersion while cloudy-white titanium oxides settle down on the bottom [113]. For Ti_3CNT_x, ammonium gas can be detected after the solution is oxidized [113].

Defects density and flake size strongly control the oxidation kinetics. Higher density of defects and smaller flake size will speed up the oxidation of MXene dispersions. Since oxidation is more intense on the edges of the flakes, capping the edges with polyanionic salts (such as polyphosphates, polysilicates or polyborates) can effectively mitigate the oxidation [114,115]. Furthermore, treating MXenes with sodium L-ascorbate can improve their oxidation stability based on the same edge-capping mechanism by the ascorbate anions [116]. Although these technique are effective, removing the added salts to restore the intrinsic MXene properties complicates the whole process.

Dispersing MXene nanosheets in non-aqueous polar solvents, such as NMP, DMSO, ethanol, etc., can minimize their interactions with water and/or dissolved oxygen, extending their shelf life. Potential good solvents are those possessing a high surface tension, a high boiling point, and a high dielectric constant, which are able to stabilize MXene nanosheets [117]. Preparation of organic MXene dispersions can be achieved through multiple solvent exchange (3 times) without sonication [118]. Improving the oxidation stability by transferring to non-aqueous solvents is particularly of more interest for solution processing of MXenes since in the majority of the deposition techniques, because of the surface tension and adhesion considerations, organic dispersions are more preferred (will be discussed later).

Basics of solution processing of MXenes

Since MXenes are mainly synthesized by solution-based methods, liquid-phase fabrication techniques such as printing, or coating are preferable for their further processing (e.g. device fabrication). Through these techniques, stable MXene dispersions are processed into continuous films with acceptable adhesion to the target substrate. Such a dispersion is called an ink and conventionally contains additives (e.g. binders, surfactants) for improving its processability and film formation behavior [119]. In most of the cases, additives degrade the electronic properties of the films/structures and should be removed at the end of the fabrication process. However, due to the presence of abundant surface functional groups on MXenes, the formulation of additive-free MXene-based inks is easier than most other materials [27]. The colloidal stability, rheological properties, and film formation behavior of MXene inks are mainly governed by the type and concentration of the surface groups. The surface tension and adhesion of the inks which mainly depend on the properties of the selected carrier solvent (the dispersion media) are also indirectly dictated by the surface groups (through MXene-solvent interactions). Hence, the properties of MXene inks are mainly determined by the physicochemical properties of the MXene itself, and the carrier solvent. Even though each process-

ing technique require an ink with specific properties (and hence, different composition), there are some general considerations in ink formulation which will be discussed here before reviewing the details of each technique. In order to maintain the continuity of the text and aid the readers with better comprehending the following discussions, basics of viscoelastic behavior of inks and surface energy related issues are also concisely reviewed.

Wettability, adhesion, and film formation of MXene inks

The interactions between inks and substrates (wettability and adhesion) are mainly depending on their surface energies and can be described by Young's and Dupre's equations,

$$\gamma_{sg} = \gamma_{sl} + \gamma_{lg}\cos\theta \text{ Young's} \tag{9}$$

$$W_{sl} = \gamma_{sg} + \gamma_{lg} - \gamma_{sl} \text{ Dupre's} \tag{10}$$

where W, γ, and θ are work of adhesion, surface energy, and contact angle, respectively [120]. These equations suggest that for a good wetting ($\theta \to 0$), the surface energy of the carrier solvent should be lower than the surface energy of the substrate ($\gamma_{lg} < \gamma_{sg}$; inferred from Young's equation), and for a good adhesion ($0 < W_{sl}$), the interfacial energy between the ink and the substrate should be lower than the sum of their individual surface energies ($\gamma_{sl} < \gamma_{sg} + \gamma_{lg}$; inferred from Dupre's equation). However, it is very important to note that these requirements are necessary but not sufficient for having a good wetting and adhesion. The reason lies in the origin and nature of the surface energy. In any material, the surface atoms, compared to the bulk atoms, are under-coordinated, which is thermodynamically unfavorable. Hence, there is always a tendency in materials to minimize this additional energy (surface energy) either by reducing the surface area or by saturating the surface dangling bonds [121]. An ideal case for saturation of the surface atoms is the formation of a bond with similar characteristics of the bonds in the bulk of that material. Hence, good wetting and adhesion to the substrate are only achieved when, in addition to the total surface energies, the individual components of the surface energies (disperse, polar, hydrogen, etc.) of the ink and substrate also match with each other (Fig. 2a).

While substrate wettability can be qualitatively examined by a simple contact angle measurement, it is more convenient to plot the wetting envelopes of that substrate using a quantitative surface energy model (e.g. Owens, Wendt, Rabel, and Kaelble model; OWRK model) [122,123]. To plot the wetting envelopes, polar and disperse components of the surface energy of the substrate should be determined first. This can be done by the application of the OWRK model and two probe liquids with known polar and disperse components (e.g. water and diiodomethane). According to the OWRK model, the interfacial energy between a solid and a liquid (γ_{sl}) can be interpreted as the geometric mean of the disperse part (γ^D) and the polar part (γ^P) of the surface energy [124,125]:

$$\gamma_{sl} = \gamma_s + \gamma_l - 2\left(\sqrt{\gamma_s^D\gamma_l^D} + \sqrt{\gamma_s^P\gamma_l^P}\right) \tag{11}$$

By substituting the γ_{sl} in Young's equation (equation (9)) from equation (11) and rearranging it according to the unknown values (γ_s^D and γ_s^P), the following linear equation ($Y = ax + b$) can be obtained:

$$\frac{\gamma_l(1+\cos\theta)}{2\sqrt{\gamma_l^D}} = \sqrt{\gamma_s^P}\frac{\sqrt{\gamma_l^P}}{\sqrt{\gamma_l^D}} + \sqrt{\gamma_s^D} \tag{12}$$

By plotting $\frac{\gamma_l(1+\cos\theta)}{2\sqrt{\gamma_l^D}}$ versus $\frac{\sqrt{\gamma_l^P}}{\sqrt{\gamma_l^D}}$ for at least two probe liquids (for which, γ_l^P and γ_l^D are known) and fitting a line to the obtained points, the slope and intersection point with the Y axis ($x = 0$) will give the γ_s^D and γ_s^P, respectively (Fig. 2b). Once γ_s^D and γ_s^P for a substrate is determined, equation (12) can be used for plotting the wetting envelopes for every chosen contact angle (Fig. 2c).

Now, without direct measurements, the contact angle of any ink (liquid or liquid mixture) can be easily estimated by locating it between different wetting envelopes (each corresponding to a specific contact angle; θ) based on its surface tension components (γ_l^D and γ_l^P). Hence, a wetting envelope plot can provide ink developers with guidelines for the selection of the carrier solvent (or solvents mixture) [126]. The usefulness of these plots in ink formulation becomes clearer when considering the fact that the colloidal stability of MXene dispersions also highly depends on the surface tension components of the carrier solvent (will be discussed later). We note that another significant advantage of using wetting envelopes for designing inks, is the ability to adjust the contact angle to a specific value [123]. This is important since complete wetting ($\theta = 0$) is not always desirable (e.g. for fine-line printing) as it leads to uncontrolled spreading of ink (Fig. 2d).

When optimizing the composition of an ink, together with the wettability and adhesion, the drying behavior of the ink should also be considered. For instance, as shown in Fig. 2e, assuming a droplet of a well-wetting ink (with pinned edges) is placed on a substrate, due to the uneven evaporation of the solvent from the sides (because of the higher surface area to volume ratio), an outward flow from the center of the droplet to the edges is generated to replenish the evaporated solvents, in particular in low viscosity inks. Such a flow carries and accumulates the particles on the edge of the droplet and forms a ring-like structure (also known as coffee-ring) [127]. This problem can be addressed by the application of multicomponent carrier solvents for ink formulation. Due to the disparity of evaporation rate of different components in the inks, surface tension, and compositional gradients form within the droplet and give rise to inward Marangoni flows, creating a more uniform redistribution of the particles [119] (Fig. 2f).

Despite the great ability of water in dispersing MXenes (solid loading and zeta potential of up to 70 wt.% and −80 mV, respectively), considering the aforementioned requirements for surface energy of inks, it cannot be a suitable carrier solvent for the formulation of MXene inks, especially for polymeric substrates. In conventional inks, additives (e.g. surfactants) are used to address the surface energy mismatches; however, in the case of MXenes, due to their oxidation sensitivity, formulation of additive-free dry-only inks is crucial. In other words, due to the restriction of employing additives, methods available for the production of stable dispersions (which are necessary for ink formulation), are thus limited. Minimization of the energetic cost of the delamination process by matching the surface tension of the dispersion media with the surface energy of the target material (here MXene) is a promising approach for the production of 2D materials dispersions [128]. When MXene is delaminated and dispersed in a solvent (or solvent mixture), a huge number of new

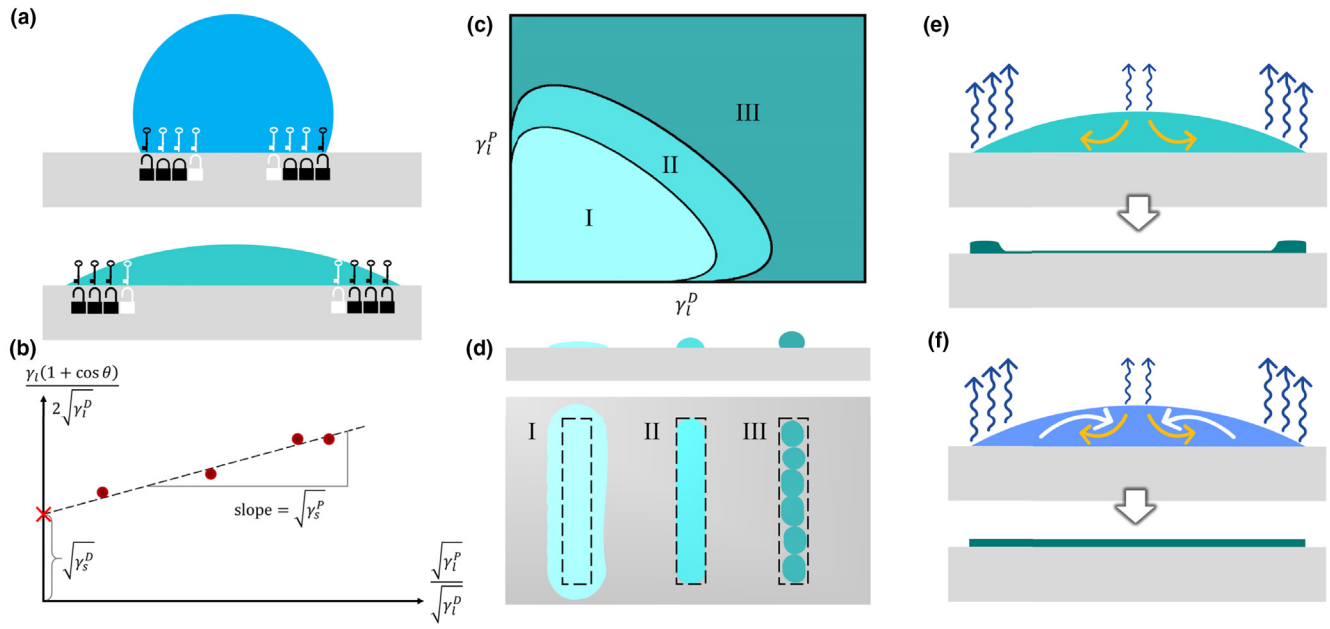

FIGURE 2

Basic surface energy characterizations and drying behavior of inks. (a) Schematic illustration of the interactions between the surface energy components of an ink and a substrate. Although total surface energies are equal in both cases, only the ink with matching surface energy components can properly wet the substrate. Keys and locks with different colors are symbolically used to convey this message that: only matching keys can unlock the locks. (b) Calculation of the surface energy components of a substrate (γ_s^D and γ_s^P) by OWRK method. (c) A schematic example of wetting envelope plots (with envelopes for two different wetting angles). (d) Effect of ink-solvent interactions; (I) strong interaction with complete wetting is not suitable for fine-line printing; (II) an optimum interaction leads to high-fidelity printing; (III) weak interaction leads to dewetting. (e) Schematic illustration of uneven evaporation of solvent from edges of a droplet and formation of a coffee-ring structure. (f) An inward Marangoni flow (by addition of a co-solvent) can redistribute the particles more evenly which leads to the formation of flat and homogenous films.

surfaces are generated which increases the interfacial energy of the system. This excess energy is the driving force for the aggregation of the dispersions, and its minimization can slow-down the aggregation process. Hence, all the discussions in matching the surface energy of the ink and the substrate are also valid here. However, unfortunately, the determination of the surface energy components (SECs) of the 2D materials (MXene) is not as straightforward as the substrates. Furthermore, variations in the SECs of the particles (MXenes) are usually synthesis route-dependent, which makes their determination even more challenging.

A common practice in the estimation of the SECs of a 2D material is based on the comparison of stabilized concentrations of dispersions in various solvents (with different SECs). Higher concentration refers to better matching and closer estimation to the intrinsic SECs of the 2D material (Fig. 3a). In the case of $Ti_3C_2T_x$ MXene, it is found that the optimal parameters include surface tensions between 35 and 42 mN/m and the ratio of polar/dispersive components between 0.61 and 0.87 (Fig. 3b), whereas the ability of the solvent to form hydrogen bonds is not necessarily important [117]. For instance, solvents like propylene carbonate, NMP, DMF, and DMSO are good carrier solvents for the $Ti_3C_2T_x$ MXene. It is also shown that the synthesis route and types of the surface groups of MXene have considerable effects on its dispersibility, which allow the utilization of different types of solvents for ink formulation through modification of the MXene surface chemistry [117]. With such an approach, it is even possible to transform the hydrophilic MXene to hydrophobic and disperse it in organic solvents. For instance, terminal groups of MXenes (-OH, -O, -F) can be replaced with long hydrophobic alkyl chains by treating the MXene with an alkylphosphonic acid (e.g. dodecylphosphonic acid; $C_{12}PA$) [129]. The resulting surface-modified MXene which can be dispersed in nonpolar solvents (e.g. chloroform) exhibits decent colloidal and chemical (oxidation) stability. However, the surface functionalization slightly degrades the electrical conductivity as insulating alkylphosphate ligands grafted on the MXene flakes, slightly disturb the electronic conduction (Fig. 3c).

Colloidal and rheological properties of MXene inks

Particle-based inks (including MXene inks) are complex fluids and exhibit intricate mechanical responses to applied stresses (or strains) mainly due to the geometrical constraints imposed by the particles. Therefore, understanding the rheological behavior of these inks is crucial for their proper processing. Indeed, during all stages of solution-based processes, from storage to application, and drying, inks are under various types of stresses and their rheological properties determine their behavior at each stage. MXene inks can offer a broad spectrum of rheological properties. This is due to the extensive effect of MXene concentration on the flow behavior of the inks (will be discussed later with more details), and the exceptional dispersibility of MXenes which leads to stable dispersions with a wide range of concentrations. To better understand the diverse rheological behavior of MXene inks, it is helpful to first review the viscoelastic properties

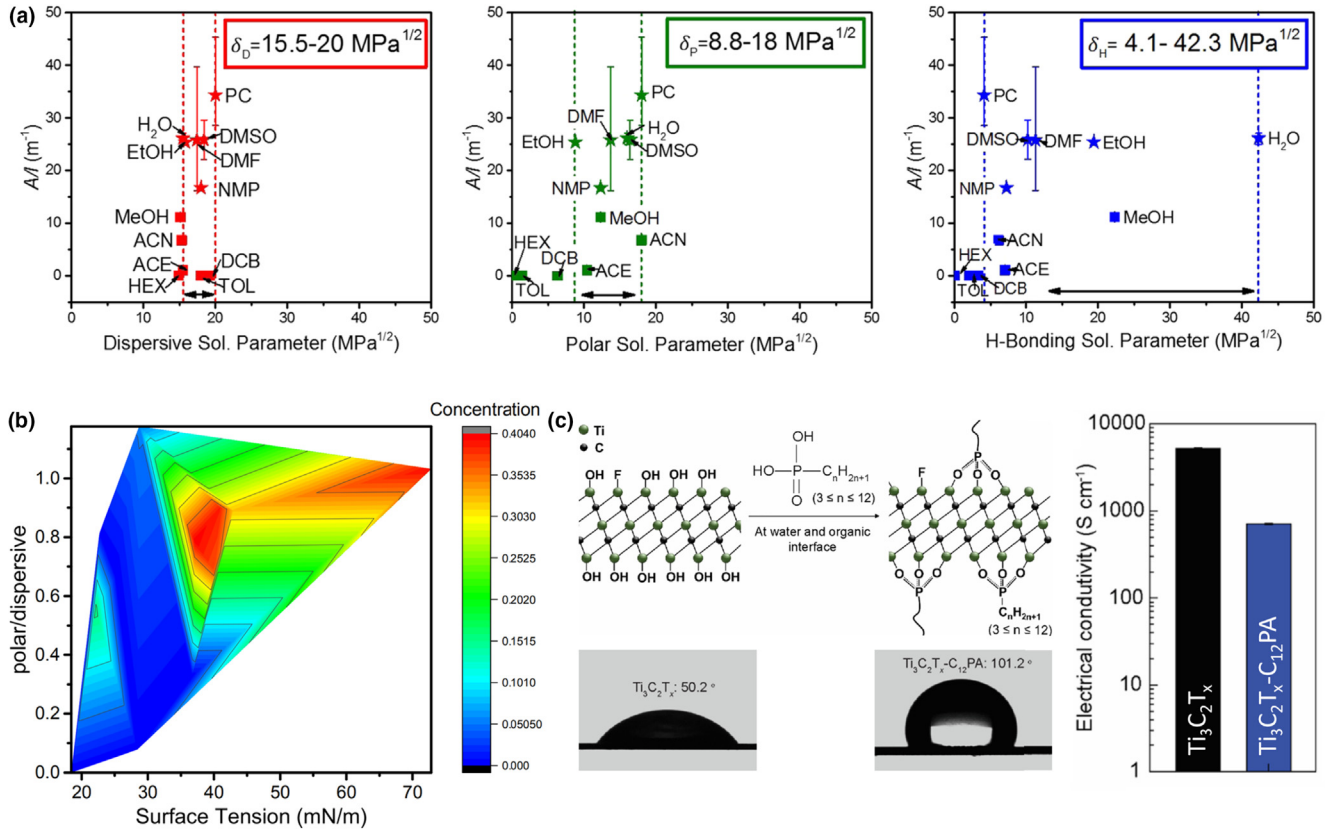

FIGURE 3

Surface energy of MXenes and their dispersions. (a) Relationships between $Ti_3C_2T_x$/solvent absorbance per cell path length (A/l) at 800 nm supported by a solvent and its Hansen solubility parameters: dispersive, polar, and hydrogen bonding, respectively. Star data points represent data for "good" solvents. Reproduced from ref [117] with permission from American Chemical Society. (b) Surface tension and Hansen polar solubility parameter divided by Hansen dispersive solubility parameter are plotted with concentration of $Ti_3C_2T_x$ in each solvent. The red areas are associated with higher concentrations and the blue areas are for lower concentrations. Reproduced from ref [117] with permission from American Chemical Society. (c) Schematic illustration of simultaneous interfacial chemical grafting reaction and phase transfer for preparing a stable nonpolar $Ti_3C_2T_x$ dispersion; Contact angle measurements for pristine $Ti_3C_2T_x$ and $Ti_3C_2T_x$-C_{12}PA films at room temperature; Electrical conductivity of pristine $Ti_3C_2T_x$ and $Ti_3C_2T_x$-C_{12}PA films. Reproduced from ref [129] with permission from American Chemical Society.

of particle-based inks and their conventional characterization methods.

All particulate inks are viscoelastic materials, meaning that their rheological behavior has both viscous and elastic characteristics. Pure carrier solvents are ideal Newtonian fluids with completely viscous behavior [130]. When deformed, their deformation rate (strain rate; $\dot{\gamma}$) is linearly proportional to the applied stress ($\dot{\gamma} = \phi\tau$), and the proportionality coefficient (fluidity) is the reciprocal of their viscosity (Fig. 4a). The deformation is irreversible, and all the applied energy dissipates as heat [131]. By the addition of solid particles, due to the particle–particle and particle-solvent interactions, the flow behavior of the carrier solvent starts to deviate from the Newtonian fluids and its viscosity becomes shear-rate dependent (Fig. 4a). In typical inks, increasing the shear rate decrease the viscosity (also known as shear-thinning). In addition to the viscous behavior, these inks show some elastic behavior as well, meaning that a part of the deformation energy can be stored in the inner structure of the ink. By further increasing the solid content and percolating the particles, sol–gel transition (fluid-like behavior to solid-like behavior) occurs and inks exhibit non-zero yield stress at zero shear rate (Fig. 4a). In this case, there is a range of strains (starting from rest) at which the elastic behavior of the inks dominates their viscous behavior [132]. Depending on the desired deposition technique, gelation can be both detrimental (e.g. inkjet printing) and beneficial (e.g. 3D extrusion printing). Therefore, determination of the composition (solid content) at which, the sol–gel transition occurs and understanding the effect of different parameters on it (e.g. particle's aspect ratio, solvent type) are of great importance for ink formulation.

The rheological properties of inks can be studied by numerous instruments and methods, but the most informative characterization is done by rheometers (especially by dynamic shear rheometers, DSR). The most commonly used experiments are rotational and oscillatory tests which are carried out by various geometries (e.g. concentric cylinder or cone and plate, Fig. 4b) depending on the specific properties of the inks and the required information. Rotational tests are mainly used for plotting the flow curves. First, the shear rate is continuously increased, and the required torque is recorded. Then the viscosity is calculated from the torque data and plotted versus shear rate ($\eta = \frac{\tau}{\dot{\gamma}}$; the torque and τ relation depends on the measurement geometry). A typical flow curve when plotted in a log–log scale has three main

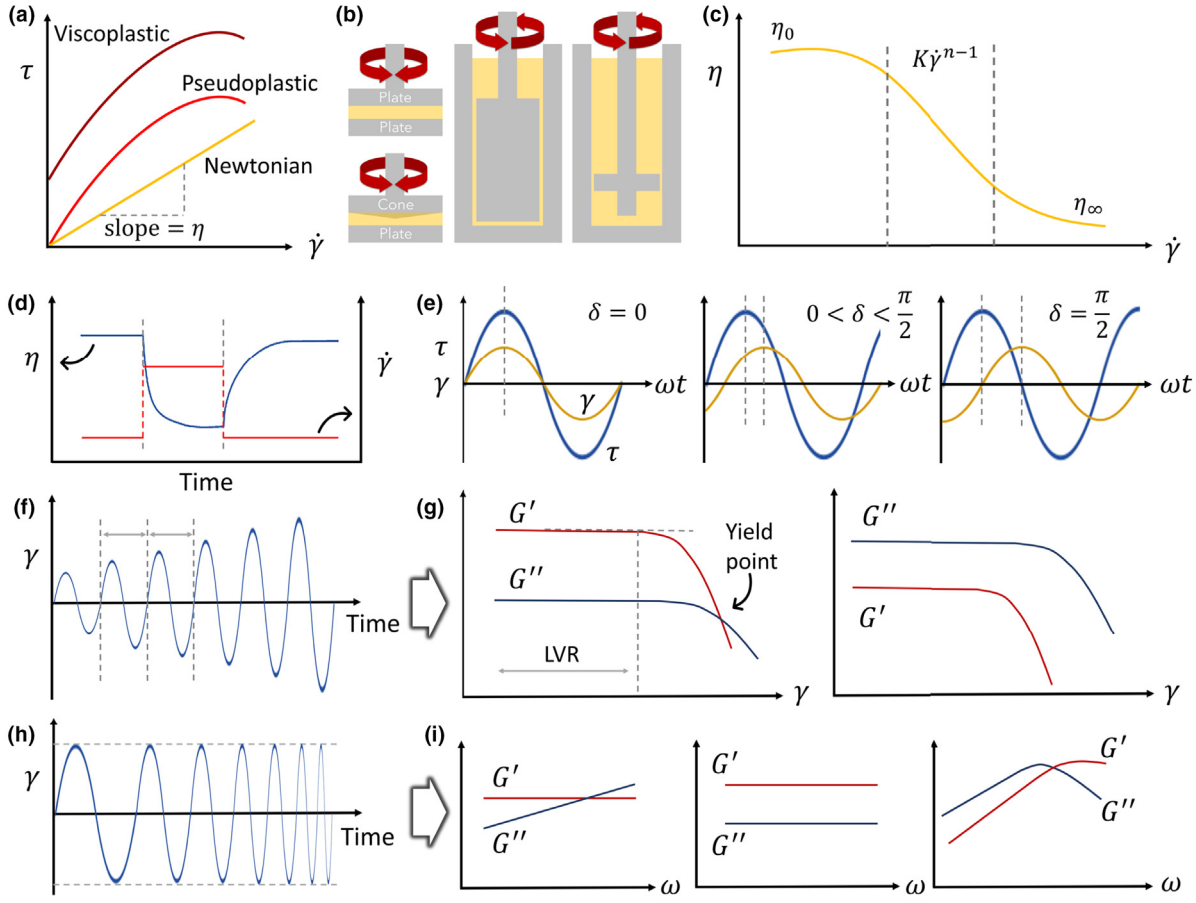

FIGURE 4

Basic rheological characterizations of inks. (a) Relation between shear stress and strain rate for three main types of inks (fluids). (b) Four different measurement geometries for a rheometer; left top: plate-plate, left bottom: cone-plate, middle: concentric cylinder, right: spindle type. (c) A typical flow curve for a power-law shear-thinning ink. (d) Three interval thixotropy test. (e) Phase shift between the maximum strain and maximum stress for a viscoelastic material (middle) in an oscillatory test. (f, g) Preset (strain) of an amplitude sweep test and two possible responses (read-outs). (h, i) Preset (strain) of a frequency sweep test and three possible responses (read-outs); (i) left: a viscoelastic solid, middle: a gel, and right: a viscoelastic liquid.

TABLE 1

Range of shear rates at different stages/methods of processing [134].

Process	Shear rate, $\dot{\gamma}$ [s^{-1}]	Process	Shear rate, $\dot{\gamma}$ [s^{-1}]
Sedimentation of particles	$\leq$ 0.001 . . . 0.01	Extrusion	10 . . . 1000
Surface leveling of coatings	0.01 . . . 0.1	Coating, printing, rolling, blade coating (manually)	100 . . . 10,000
Sagging of coatings, dripping, flow under gravity	0.01 . . . 1	Spraying	1000 . . . 10^4
Dip coating	1 . . . 100	Blade coating (machine), high-speed coating	1000 . . . 10^7

regions: low shear, power-law, and high shear (Fig. 4c). In low and high shear regions, the ink behaves like Newtonian fluids and the viscosity is shear-rate independent (plateau). In the power-law region (also known as Ostwald–de Waele power-law), the viscosity is given by equation (13) in which, K and n are the flow consistency and flow behavior indices, respectively [133].

$$\eta_{eff} = K\dot{\gamma}^{n-1} \tag{13}$$

For a Newtonian fluid, the flow behavior index (n) is equal to 1, for a dilatant fluid (shear-thickening) it is larger than 1 (usually not favorable for solution processing), and for a pseudoplastic fluid (shear-thinning) it is smaller than 1. Hence, n, which is the slope of the linear section of the flow curves (in log–log scale) in the power-law region, can be used for comparison of the pseudoplasticity of different inks. Flow curves are especially useful for the determination of the processability of an ink for a specific method, as each shear rate (and the behavior of the ink at that shear rate) can be correlated with a specific processing technique (Table 1).

The viscosity of some non-Newtonian fluids, after a deformation and removal of the stress (or reduction of its level), may not immediately recover to its initial value (which is called thixotropy). Thixotropy can be studied by another type of rotational

test in which, the ink is subjected to two different levels of shear strain within three successive time intervals (1st: low shear, 2nd: high shear, and 3rd: same low shear as the 1st interval; Fig. 4d), and the viscosity changes are monitored. While this property is useful in some solution-based processes (e.g. leveling of the films), it can be detrimental in some others (e.g. 3D extrusion printing).

While rotational tests provide valuable information about the rheological properties of the inks, the viscous and the elastic components of the flow behavior cannot be distinguished. For this purpose, oscillatory tests are developed (Fig. 4e) in which, a sinusoidal strain (equation (14)) is applied to the ink, and corresponding required stress is measured (equation (15)). For an ideally elastic material (consider a spring), the maximum stress is observed at the maximum strain (no phase shift; $\delta = 0$), while for a purely viscous material (consider a dashpot), the maximum stress is experienced at the beginning of the deformation (minimum strain, which corresponds to a $\frac{\pi}{2}$ phase shift). For a viscoelastic material, this phase shift locates between two extremes ($0 < \delta < \frac{\pi}{2}$), and $\delta = \frac{\pi}{4}$ represents the sol–gel transition point ($0 < \delta < \frac{\pi}{4}$ corresponds to solid-like behavior, and $\frac{\pi}{4} < \delta < \frac{\pi}{2}$ corresponds to fluid-like behavior). Now it is possible to study the viscous and elastic components of the flow behavior separately as shown in equations (14) and (15) where, γ_0, τ_0, and ω are strain amplitude, stress amplitude, and angular frequency, respectively. The first term in equation (15) ($G^{'}(\omega)\gamma_0 \sin \omega t$) is in-phase with the deformation and represents the elastic behavior and the second term ($G^{''}(\omega)\gamma_0 \cos \omega t$), which is out-of-phase, corresponds to the viscous behavior of the ink. $G^{'}$ and $G^{''}$ are elastic and loss moduli (respectively) and are extensively used for the evaluation of the ink behavior in all oscillatory tests [135].

$$\gamma(t) = \gamma_0 \sin \omega t \Rightarrow \dot{\gamma}(t) = \gamma_0 \omega \cos \omega t \tag{14}$$

$$\tau(t) = \tau_0(\omega) \sin [\omega t + \delta(\omega)] = G^{'}(\omega)\gamma_0 \sin \omega t + G^{''}(\omega)\gamma_0 \cos \omega t \tag{15}$$

Oscillatory rheological characterizations usually start with an amplitude sweep test (especially for gel inks) in which, the amplitude of the strain is increased at each cycle and the elastic and loss moduli are plotted versus strain or stress (Fig. 4f, g). For gel inks, the limit of the linear viscoelastic region (LVR), which is the maximum strain up to which, the ink can be deformed without destroying its internal structure can be determined by amplitude sweep tests. Yield stress of gel inks as a very important figure of merit (FOM) in some solution-based processes (e.g. extrusion printing) can also be extracted from amplitude sweep tests. After the determination of the LVR, another important oscillatory characterization, the frequency sweep test, can be carried out. In frequency sweep tests, a deformation with an amplitude smaller than the LVR is applied and the elastic and loss moduli are plotted versus the frequency (Fig. 4h, i). The response of the sample at high and low frequencies represent the short- and long-term behavior of the ink, respectively [136].

The rheological properties of MXene dispersions have been extensively investigated, and the concentration of MXene, as well as its aspect ratio, are found to be the most important factors in the determination of the flow behavior [36,137,138]. Single-layer MXene dispersions (average flake size ~ 1 μm), in contrast to their multi-layer counterparts and even other types of nanomaterials, exhibit a very steep viscosity rise by increasing their concentration (or volume fraction), mainly due to the very high aspect ratio of the flakes (Fig. 5a) [137]. While this behavior limits the formulation of high-solid-content inks, which is necessary for some applications (e.g. energy storage), it provides a unique opportunity for the deposition of thin and transparent films. Surprisingly high levels of elastic behavior have been observed in dilute dispersions of MXene (even as low as 0.36 mg ml^{-1}) which is beneficial for thin-film processing methods such as spin- and spray-coating [76,139] as it assists with the elimination of process-imposed perturbations [140]. By increasing the MXene concentration to 0.9 mg/mL (close to the sol–gel transition point), a volume-spanning percolating network starts to form within the system, which is reflected in the soft-solid-like behavior of the dispersion at low frequencies and fluid-like behavior (power-law scaling) at high frequencies (Fig. 5b). This rheological behavior could be suitable for techniques such as inkjet printing (will be discussed later) in which, the ink should become jettable under application of the shear stress and be able to regain its viscosity and rigidity after the deposition (at rest). At higher concentrations, $G^{'}$ becomes frequency-independent and its crossover point with $G^{''}$ shifts to higher frequencies. This rheological behavior resembles that of soft gels [141]. Similar trend but at much higher concentrations in the rheological behavior of multi-layer MXene is also observable (Fig. 5c–f).

When developing an ink for a specific application, the substantial difference in the rheological properties of single- and multi-layer MXenes is the first parameter for consideration. For instance, if deposition of a thick film is required, the ultra-high viscosity of the high concentration single-layer MXene inks will render them unprocessable with the majority of the solution-based techniques. In contrast, for achieving the highest possible transparency in the deposited films, defect-free large flakes of single-layer MXene would be the best choice. Once the material is selected according to the application, then the deposition technique should be chosen. Numerous parameters, such as fabrication throughput, resolution, and ability of contact/non-contact deposition should be considered in this stage. As such, a "property-process map" is plotted in Fig. 6, as guidelines for MXene processing. Using this map and considering the desired properties (i.e. resolution, conductivity, film thickness, or film transparency) and expected throughput, one is able to locate the most suitable processing technique and corresponding viscoelastic properties of the ink.

Since the rheological properties of the inks can be easily adjusted by changing the solid content, inks for various processing methods can be formulated accordingly. Due to the dependence of the rheological properties to other factors such as nanosheets' aspect ratio and the selected carrier solvent, concentration vs. viscosity relation should be determined individually for every specific system. It should be also noted that the viscosity values can only provide rough estimations on the processability of the inks since steady-state rheological properties (e.g. viscosity) are not usually sufficient for the determination of the optimum ink/printing parameters [142]. Hence, the dynamic rheological properties should also be considered for processability evaluations.

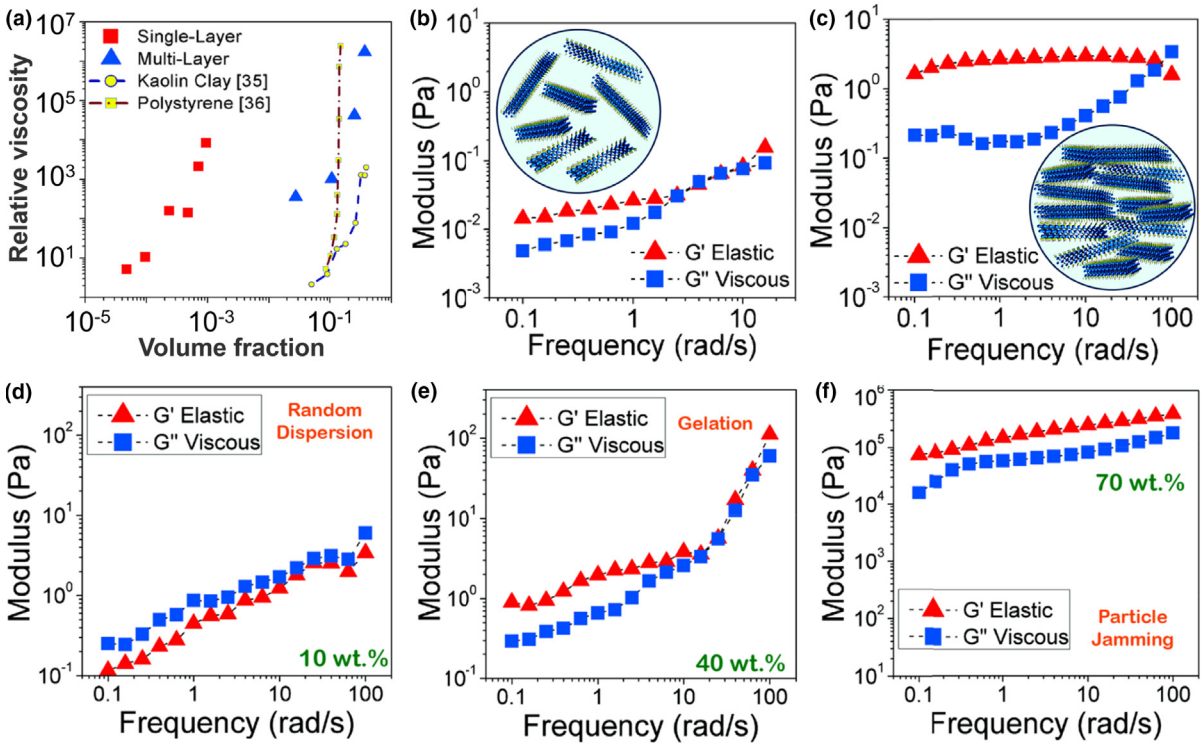

FIGURE 5

Rheological properties of MXene dispersions. (a) Relative viscosity versus volume fraction plot for single- and multilayer $Ti_3C_2T_x$ dispersions. Along with the same data for polystyrene and kaolin clay (for comparison). (b, c) Plots showing viscoelastic measurements conducted on single-layer MXene suspensions at various concentrations: (b) 0.9 mg mL^{-1} and (c) 3.6 mg mL^{-1}. (d–f) Plots showing viscoelastic measurements conducted on multilayer MXene dispersions at various solid loadings: (d) 10 wt.%, (e) 40 wt.%, and (f) 70 wt.%. All the figures are reproduced from ref [137] with permission from American Chemical Society.

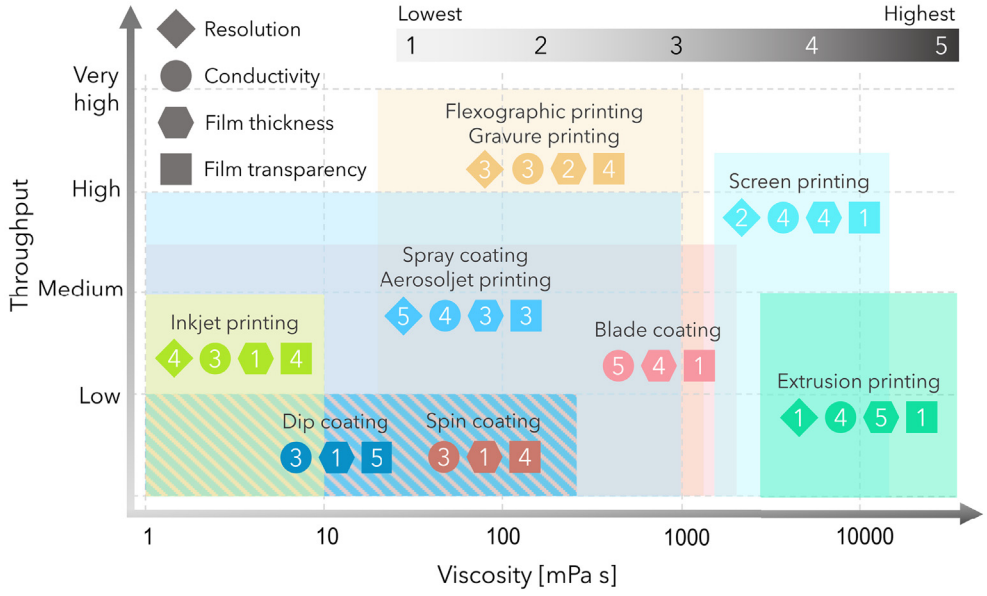

FIGURE 6

The map of guidelines for solution processing of colloidal MXenes. Relation between the throughput, ink viscosity, resolution (only applies for printing methods), film conductivity, film thickness and film transparency for major printing/coating methods are provided.

Printing of MXenes

Printing is an additive manufacturing technique that offers enormous possibilities for simple, large-scale, and low-cost device fabrication [143]. Compared to conventional silicon-based electronics or gas-phase deposition techniques which require sophisticated and lengthy manufacturing processes, printing is done in a maximum of three steps: pretreatment of the substrate, printing, and post-treatment (ideally only drying; sometimes

heat treatment). Despite the great advancements in printing technologies, functional printing and ink development are still in their infancy. This is mainly due to the difficulty of developing additive-fee, high-performance inks. However, MXenes can change the game by offering exceptional possibilities for the production of such inks (as discussed before). Since MXenes are in their early stages of development, their printing is currently limited to the techniques which are frequently used and are available in the research labs. So far, only three printing methods including inkjet-, screen-, and extrusion-printing have been reported for processing MXenes which will be reviewed here.

Inkjet printing

Inkjet printing (IJP) is a digital non-contact method, which is vastly used in both research and industry. IJP is one of the best techniques for parameter optimization, and fast prototyping since the printing pattern is provided to the printer as a digital file (can be modified easily) and ink consumption is very low (1–2 mL) [144]. Based on the droplet generation mechanism, there are two main types of inkjet printing, continuous inkjet printing (C-IJP) and drop-on-demand inkjet printing (DOD-IJP) [145]. C-IJP is mostly used in industry while DOD-IJP is more suitable for research purposes. In C-IJP, drops are continuously formed by the Rayleigh instability of a liquid column that is ejected under pressure through a small nozzle. A small potential is applied to the ink to slightly charge the generated droplets. Due to their charge, unwanted droplets (according to the printing pattern) can be deflected by an electric field into a gutter (Fig. 7a). The size of the droplets is about 100 μm which is bigger than DOD-IJP (20–50 μm). In DOD-IJP, as its name implies, droplets are generated when they are needed (according to the printing pattern). Jetting is done by the propagation of a pressure pulse in the ink reservoir behind the printing nozzle (Fig. 7b). The pressure pulse can be generated by two methods: heating of a thin film which leads to the formation and bursting of a bubble in the ink, or by direct mechanical actuation using a piezoelectric transducer [145].

Droplets formed in DOD-IJP have a characteristic shape (Fig. 7c). First, the ink column thins to form the main leading droplet which is usually associated with an elongated tail or ligament. Rupture of this tail can lead to the formation of a smaller droplet which follows the main drop (therefore known as satellite drop) and can often merge with the main drop if the flying distance between the printing head and the substrate is enough. However, if it lands as a separate droplet on the substrate, noncircular and irregular patterns with a deleterious influence on deposit precision, resolution, and accuracy will form [145]. The droplet formation and its properties, including velocity and size, heavily depend on the shape and amplitude of the pressure pulse which can be easily tuned in piezoelectric DOD-IJPs. Jettability of the inks and properties of the droplets, in addition to the printer's operational parameters, are heavily dependent on the surface tension and rheological properties of the inks. Almost all stages of the IJP, including droplet formation (depends on the surface tension and velocity of the drop), stable jetting, the formation of satellite droplets, and even drop splashing upon

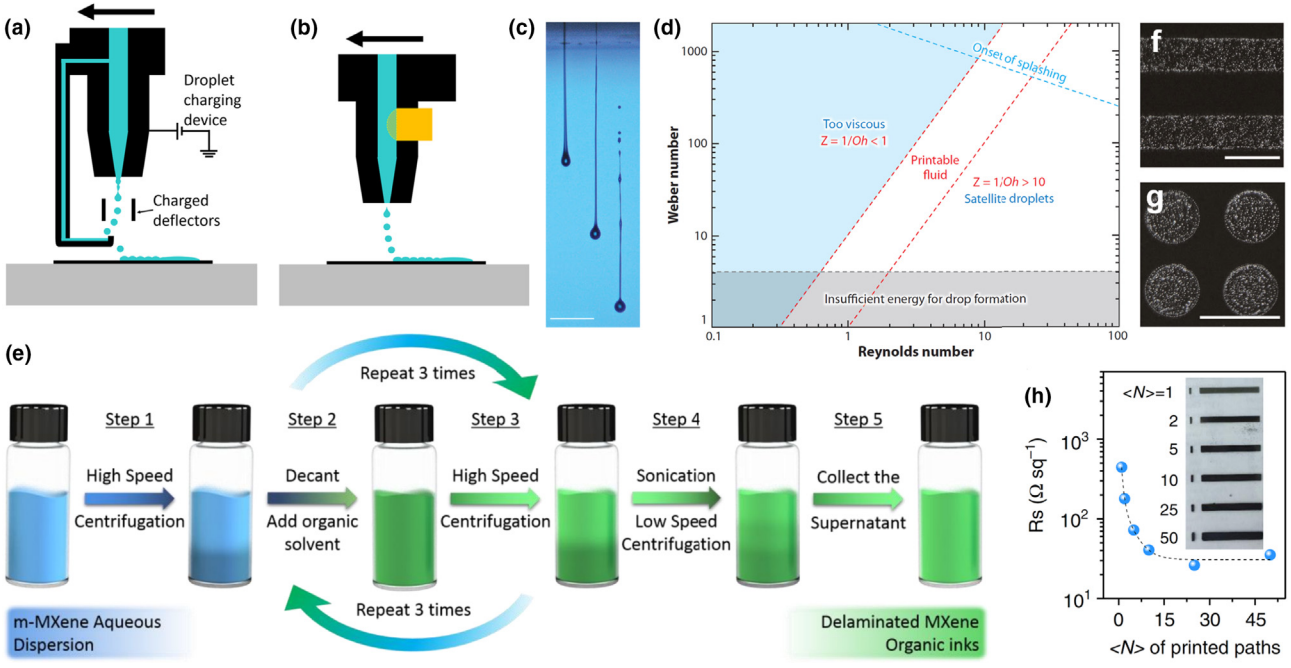

FIGURE 7

Inkjet printing of MXenes. (a, b) Schematic diagram showing the principles of operation of (a) a continuous inkjet (CIJ) printer, and (b) a drop-on-demand (DOD) inkjet printing system. (c) A high-speed photographic image showing three drops ejected from a DOD printer at different stages of drop formation (scale bar: 200 μm). (d) Processing window for formulation of inkjet printable inks. Reproduced from ref. [145] with permission from Annual Reviews. (e) Transferring MXenes to organic solvents by repeated centrifugation/redispersion. Reproduced from ref. [35] with permission from Springer-Nature. (f, g) Inkjet printed dots and stripes by MXene inks (in IPA) with negligible coffee-ring effect. Reproduced from ref. [91] with permission from Springer-Nature. (h) The sheet resistance, R_s, plotted as a function of printing pass. Inset shows the optical images of various printed lines (2 cm in length) with different overlayer printing Reproduced from ref. [35] with permission from Springer-Nature.

impact with the substrate, can be characterized by a number of dimensionless physical constants such as Reynolds (*Re*), Weber (*We*), and Ohnesorge (*Oh*) numbers. For stable drop formation it is found that the inverse Ohnesorge number (Z) of the ink which can be calculated by equation (18) should have a value of $1 < Z < 14$ [35,91,146]. In some references, possessing $1 < Z < 10$ is defined as preferable inks [145]. In these equations, υ, γ, ρ, a, andη are velocity, surface tension, density, a characteristic length (diameter of the nozzle in IJP), and dynamic viscosity, respectively [145].

$$Re = \frac{\upsilon \rho a}{\eta} \tag{16}$$

$$We = \frac{\upsilon^2 \rho a}{\gamma} \tag{17}$$

$$Z = \frac{1}{Oh} = \frac{Re}{\sqrt{We}} = \frac{(\gamma \rho a)^{1/2}}{\eta} \tag{18}$$

Since the formation of a new droplet is associated with an increase in the surface energy, the droplet should possess a minimum velocity (energy) to overcome the ejection energy barrier. In this regard, it is suggested that the ink's Weber number should be bigger than 4. It is also found that the splashing of an ink on a flat and smooth substrate occurs when $50 < We^{1/2}Re^{1/4}$ [145]. Considering the aforementioned guidelines, it is possible to construct a map in parameter space, with coordinates *Re* and *We*, that can be used for ink formulation for DOD-IJP (Fig. 7d).

As mentioned earlier, due to their high surface tension, aqueous MXene inks are not suitable for printing on non-porous substrates. In the case of IJP inks, the selection of carrier solvent is even more critical since the coffee-ring effect is stronger in low viscosity inks (such as IJP inks). Transferring MXenes to organic solvents can be done either by drying/redispersion [91] or repeated centrifugation/redispersion in the target solvent (Fig. 7e) [35]. It should be noted that when LiF is used for the etching process of the MAX phase, the drying/redispersion approach is not suitable since the residual Li^+ ions make the redispersion step more difficult [117]. Application of a low boiling point solvent such as isopropyl alcohol for IJP inks can considerably reduce the coffee-ring effect (Fig. 7f, g) while fulfilling the specific requirements of the IJP inks for satellite-free stable jetting (for a ~2 mg mL^{-1} ink and nozzle diameter of 22 μm: $Z \sim 8.3$). The rheological requirements of the IJP inks limit its application to low-solid-loading inks which are suitable for printing thin/transparent films/structures. Since the lateral dimensions of the as-synthesized MXene flakes are in the range of few micrometers, they can easily clog the nozzles of the printer. Hence, it is highly suggested to reduce the flake size by ultrasonic treatment to 1/50 of the nozzle diameter [91]. We note that the IJP method allows to print paths with a high resolution and line width down to 50~80 μm, and is thus extremely suitable for printing prototype devices in the lab scale. However, its working mechanism implies a low printing throughput (Fig. 6), limiting its application in scalable printed electronics.

Thanks to the exceptional conductivity of MXenes, the resistivity of the printed tracks is very low and suitable for lots of applications. By overlayer printing, the sheet resistance can be significantly decreased (down to 10 Ω sq^{-1} for a $Ti_3C_2T_x$ MXene with 5 layer overprints; Fig. 7h) [35]. The highly conductive MXene films can also provide an efficient electromagnetic interference shielding to 50 dB with a film thickness of 1.35 micrometers [34]. To leverage the excellent broadband nonlinear optical responses, the printed MXene films have been incorporated into diverse laser resonators, both fiber and solid-state configurations, to generate pulsed laser output [91]. The operation wavelength overlaps 1~3 micrometers, and the generated pulse duration can be as short as ~100 femtoseconds.

Screen printing

Unlike inkjet printing, screen printing (SP) is a fast and efficient contact printing method in which, the ink is deposited on the substrate through a mesh with some open (printing pattern) and blocked (non-printing) areas. The printing can be done in manual or automated mode, and in both cases, the printing setup is very simple and inexpensive (compared to other printing methods). SP is mainly used for deposition of thick films (1–100 μm), and if done in the flatbed automated mode (sheet-to-roll), printing speed can reach up to 70 m/s [144]. It is also possible to carry out the SP in a roll-to-roll manner which reaches higher printing speeds (up to 100 m/s) but requires a different type of cylindrical rotating screens. In the flatbed mode, the screen is placed with a small gap on the substrate (snap-off distance) and the ink is flooded over the screen to fill its openings. Then a squeegee is drawn across the screen to push out the ink and transfer it to the substrate (Fig. 8a). Considering the ease of fabrication of the screens, SP can even serve as a fast prototyping method. The fabrication of screens is simple and requires little training and tools (Fig. 8b) which makes it widely accessible.

Despite the simplicity of the printing method itself, ink formulation is very challenging due to its complex rheological requirements. Recommended viscosities for SP inks are very diverse but are usually in the range of 2–50 Pa·s (at $\dot{\gamma} = 100s^{-1}$) [142]. Inks should exhibit shear-thinning behavior, and thixotropy, to some extent would also be beneficial since it allows the ink to level-out and reduces the mesh marks on the prints. High yield stress is generally desirable since it helps the ink to stay in the openings of the screen (after flooding) and maintain its shape after deposition. The importance of proper adjustment of G' and G'' becomes more evident when considering the thickness of the wet films, which can easily spread (ink bleeding) and deteriorate the quality of the printed patterns. However, it should be noted that high G' values may result in tacky inks which hang-up on the squeegee during the printing [142]. Except for MXenes and few other materials, fulfilling these requirements is impossible without extensive application of binders and rheology modifiers. This is one of the biggest advantages of MXene for developing functional inks which can be processed at room temperature on almost any substrate.

As mentioned earlier, a slight concentration increase of delaminated MXene inks leads to a large increase in viscosity. This means that the solid loading of screen-printable delaminated MXene inks are usually much lower than other nanomaterials, which is undesirable for some applications where transferring a large amount of material is needed (e.g. energy

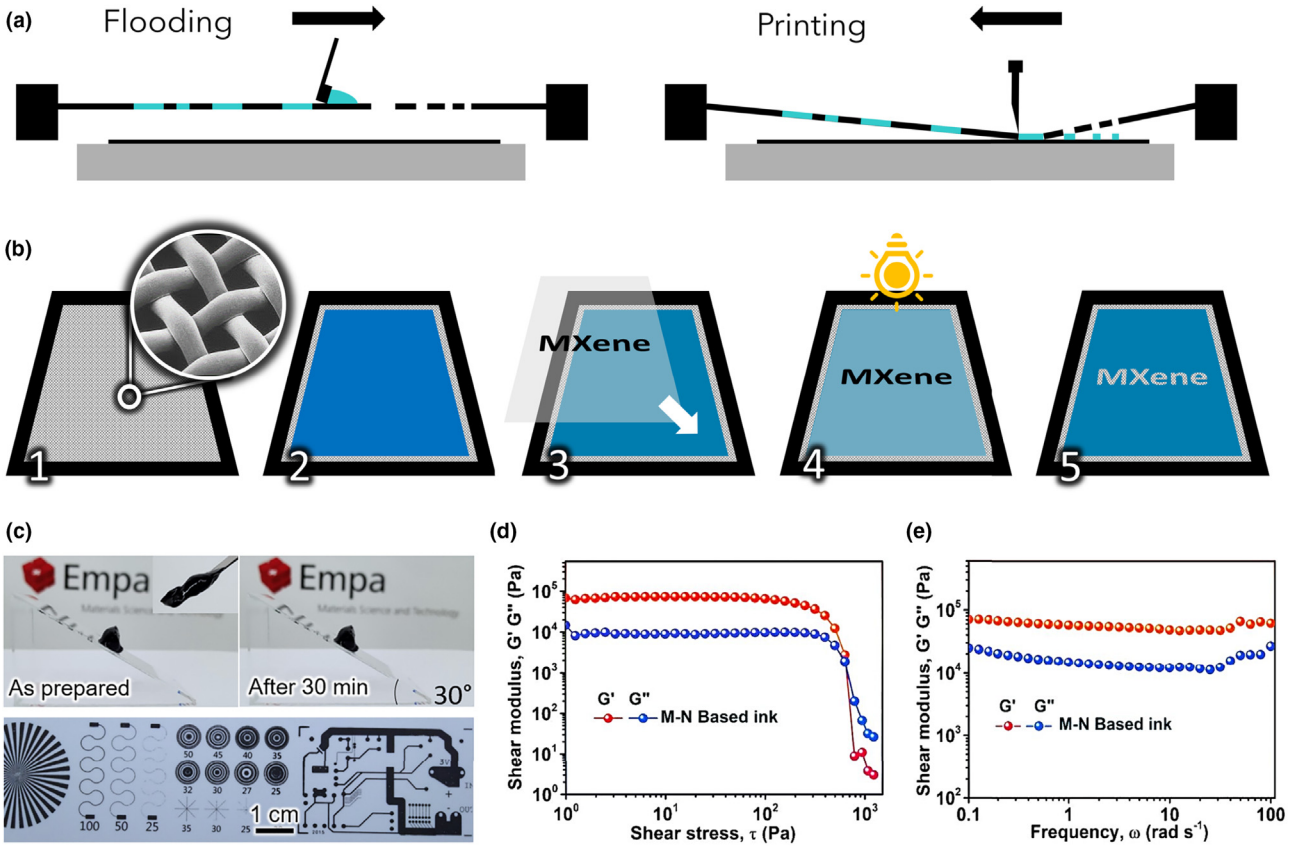

FIGURE 8

Screen printing of MXenes. (a) Left: Flooding ink over the screen to fill its openings. Right: Pushing the ink out of the screen to transfer it to a substrate. (b) Screen fabrication process: 1. Screens are made by stretching and attaching a mesh (made of silk/polymer/metal threads) to a rigid frame; 2. The mesh is coated with a water-soluble, UV-curable monomer (photo-emulsion); 3. After drying (in dark), the desired pattern which is printed on a transparent foil is placed on the mesh; 4. The photo-emulsion is polymerized by illumination of UV light, everywhere expect for the areas under the pattern; 5. The open areas of the screen (printing pattern) is obtained by washing the non-polymerized areas (monomer) with water. (c) Rheological properties (pseudoplasticity) of screen-printable sediment inks (top) and examples of printed structures (bottom). Reproduced from ref. [36] with permission from Wiley-VCH. (d, e) Rheological properties of nitrogen-doped, screen printable MXene inks: (d) Amplitude sweep test; and e) frequency sweep test. Reproduced from ref. [147] with permission from Wiley-VCH.

storage). In this case, multilayer MXene is a better choice for SP. Due to the high conductivity of the MAX phase, it is even possible to formulate high-concentration SP inks with the sediments of the MXene synthesis process which are usually discarded [36]. The rheological properties of the sediment inks fulfill the requirements of the SP inks with proper elasticity and shear-thinning behavior. Considering the low exfoliation yield of MXenes (<10–20%), this approach can significantly lower the production cost and pave the road towards commercial printing of electronics. Screen-printed structures based on MXene have been fabricated on paper with high resolution and spatial uniformity, including micro-supercapacitors, conductive tracks, integrated circuit paths (Fig. 8c). The existance of nanosheets among the layered MXene microsheets act as efficient conductive binders, maintaining the mechanical integrity and thus the metallic conductive network. An impressive sheet resistance of 2.2 Ω/sq can be achieved (16 Ω/sq for 1 pass printing; film thickness of 1.4 μm) with decent mechanical properties.

Furthermore, the nitrogen doping can improve the conductivity and redox activity of MXene and thus boost the electrochemical performance of devices. As a result, the screen printed N-doped MXene microsupercapacitor delivers an areal capacitance of 70.1 mF/cm^2 and outstanding mechanical robustness [147]. Interestingly, MXenes can exhibit these exceptional rheological properties even after functionalization/doping or hybridizing with other nanomaterials (Fig. 8d, e). Despite these progresses, formulation of screen printable MXene inks requires further attention since aqueous inks suffer from fast evaporation of the solvent (water). This leads to an increase in the viscosity of the inks and shortens the printing time which is not suitable for industrial applications. Unfortunately, organic solvents which are capable of dispersing high concentrations of MXene (e.g. NMP, DMSO) are not compatible with the conventional emulsions which are used for making SP screens. Therefore, developing organic inks in less aggressive solvents is strongly required.

Extrusion printing

In extrusion printing, a gel-like ink (solid-like behavior) is extruded as a filament through a nozzle and deposited on a substrate (Fig. 9a). It can be used for both 2D [35] and 3D [148] printing of materials, but the 3D mode requires more specific rheological properties to be able to print in a layer-by-layer man-

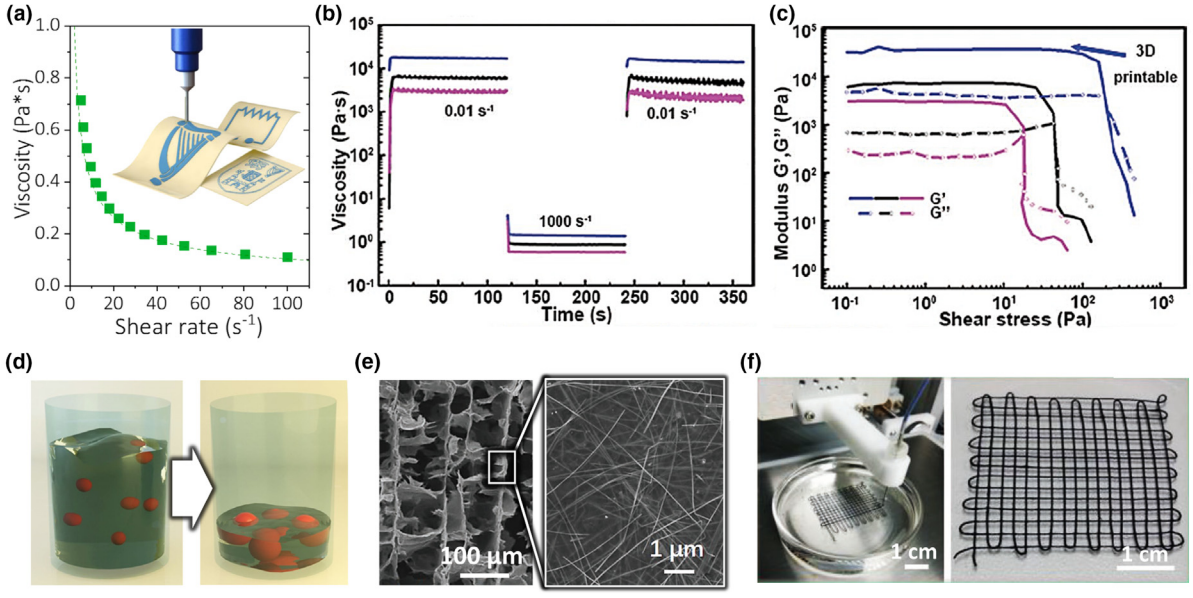

FIGURE 9

Extrusion printing of MXenes. (a) Flow curve of a 2D-extrusion printed MXene ink; inset is a schematic illustration of extrusion printing method. Reproduced from ref. [35] with permission from Springer-Nature. (b, c) Rheological properties of the 3D-extrusion printable inks: (b) Thixotropy, and (c) Yield stress tests. Reproduced from ref. [138] with permission from Wiley-VCH. (d) Schematic of the MXene solution at low and high concentrations; adding SAP beads to the dispersion resulted in a uniform concentrated MXene solution. Reproduced from ref. [149] with permission from American Chemical Society. (e) Cross-sectional SEM image and magnified cross-sectional SEM image of an extrusion-printed, freeze dried MXene-AgNW-MnONW-C_{60} composite, showing the binder-like effect of MXene. Reproduced from ref. [148] with permission from Wiley-VCH. (f) Optical images of the 3D-printed TOCNFs/Ti_3C_2 fabrics with a woodpile structure. Reproduced from ref. [150] with permission from Wiley-VCH.

ner. 2D extrusion printing is suitable for the deposition of thick films/structures with very high conductivities (Fig. 6). High yield stress (usually > 100 Pa but depends on the printer) and very little thixotropy are the two most important requirements (Fig. 9b, c). Since single-layer MXene inks have relatively low volumetric solid content (because of low concentration), considerable shrinkage can happen upon drying. To circumvent this problem and preserve the initial 3D structure, printed parts are usually freeze-dried. As a result, extremely porous structures are obtained which have vast applications in energy storage [138].

Due to the high surface charge (zeta potential) and strong repulsion of the MXene flakes in aqueous suspensions, increasing their concentration is very challenging. This problem can be solved by the application of superabsorbent polymer beads to remove the excess water and increase the concentration to as high as 290 mg/mL (Fig. 9d) [149]. This ink complies well with the predicted processing window ($2 < G'/G'' < 20$, $0.01 < \omega < 10$ Hz) for extrusion printing of the single-layer MXene. Thanks to the strong interactions between MXene nanosheets, even extremely thick (~100 μm) extrusion printed structures are robust and show great flexibility.

The exceptional film formation ability and the strong interlayer interactions of flakes make MXenes a perfect alternative for conventional binders. For instance, by the addition of MXenes to other nanomaterials which themselves, are unsuitable for the formulation of additive-free inks, 3D printable inks can be formulated (Fig. 9e). The addition of other nanomaterials such as nanowires can also increase the yield stress and improve the rheological properties of the MXene inks. Extrusion printing is a versatile method that can also be used for the fabrication of free-standing devices. For instance, a composite of MXene and cellulose nanofibrils ink can be used for printing a smart textile (Fig. 9f). For this purpose, instead of a conventional substrate, the ink is printed into an ethanol coagulation bath. Because of the rapid solvent exchange between water and ethanol within the printed ink, a continuous and stable gel fiber is obtained [150]. These smart microfibers and textiles are responsive to photothermal, electrothermal, and electromechanical stimuli.

Coating of MXenes

Besides printing strategies to fabricate MXene-based patterns and devices, coating of MXene dispersions have also been extensively studied in the past decade. For occasions requiring thin, continuous conductive films or electrodes, direct coating techniques represent promising routes with great versatility. These techniques include but are not limited to spin-casting, spray-coating, dip-coating, stamping, vacuum-assisted filtration, etc. The as-obtained MXene thin, conductive coatings can be further employed for the fabrication of high-performance, state-of-the-art functional (stretchable, bendable, and foldable) electronics.

Dip-coating

Dip-coating is known for the simplicity and potential for scalable fabrication of large-area thin films. According to the guideline map (Fig. 6), when the viscosity of MXene dispersions is low, dip-coating is recommended to give MXene films ranging from highly transparent with good conductivity to relatively thick films. MXene colloidal dispersions typically possess negative zeta

potentials (−30 to −80 mV), resulting in repulsive interactions among negatively-charged MXene nanosheets and forming stable, homogeneous dispersions that are suitable for dip-coating. In general, dip-coating can be divided into four steps, namely dipping, immersion, deposition and drainage, and solvent evaporation, as shown in Fig. 10a. Briefly, a pre-treated substrate is immersed in MXene dispersions for a certain period of time and then raise out at a constant speed by a motorized arm. Upon the removal of the substrate, a thin MXene layer deposits on the substrate while excessive dispersion returns to the bulk solution. Further evaporation leads to the formation of MXene film adhere to the substrate. As such, multiple factors govern the resultant MXene films' quality and homogeneity, i.e. MXene concentration, quality of MXene flakes, pulling speed, number of dips, immersion duration, substrate surface, and environment humidity, etc. For instance, dipping the pre-treated glass in MXene baths with concentrations of 1–10 mg/mL (flake size ∼ 1–2 μm, Fig. 10b) and pulling at a constant speed (2 mm/s) give continuous, smooth MXene films with thickness ranging from 20 nm (transparent) to 150 nm (Fig. 10c), depending on the concentration [151]. Increasing the number of dips results in thicker MXene films.

To further enable a diversity of functionalities on the device, modifying the substrate surface has been proven to be effective. It is generally known that while directly depositing MXene flakes onto hydrophobic polymer substrates is unable to produce high-quality films, hydrophilic treatment (i.e. oxygen plasma) would inevitably lead to the shrinkage of the polymer substrates, rendering the homogenous coating of MXenes on the soft polymer substrates rather challenging. To this end, imparting polymer soft substrate with a layer of positively-charged material, such as poly(diallyldimethylammonium chloride) (PDAC, zeta potential ∼ 18 mV) to allow for the layer-by-layer assembly process by electrostatic interactions, is quite promising [152]. For instance, alternatively dipping the substrate in PDAC and MXene dispersions lead to the easy fabrication of conductive, stretchable, and bendable films (Fig. 10d), based on which wearable sensors were built with excellent performance [152]. Similarly, by immersing pre-treated, NH_2-terminated PET fiber-like threads in the aqueous dispersion of MXene, MXene-coated polymer threads can be readily achieved, allowing for sewing and knitting into wearable heaters for electrothermal applications (Fig. 10e) [153].

In addition, dip-coating enables the quick deposition of high loading of MXene flakes on cellulose-based yarns such as cotton, bamboo, fibers, etc., forming conductive yarn electrodes. These cellulose substrates provide a much higher surface area than that of the planar substrate such as glass or PETs, leading to much thicker films as shown in Fig. 10f [154]. The natural hydrophilic groups on the yarns greatly facilitate the attachment of MXene

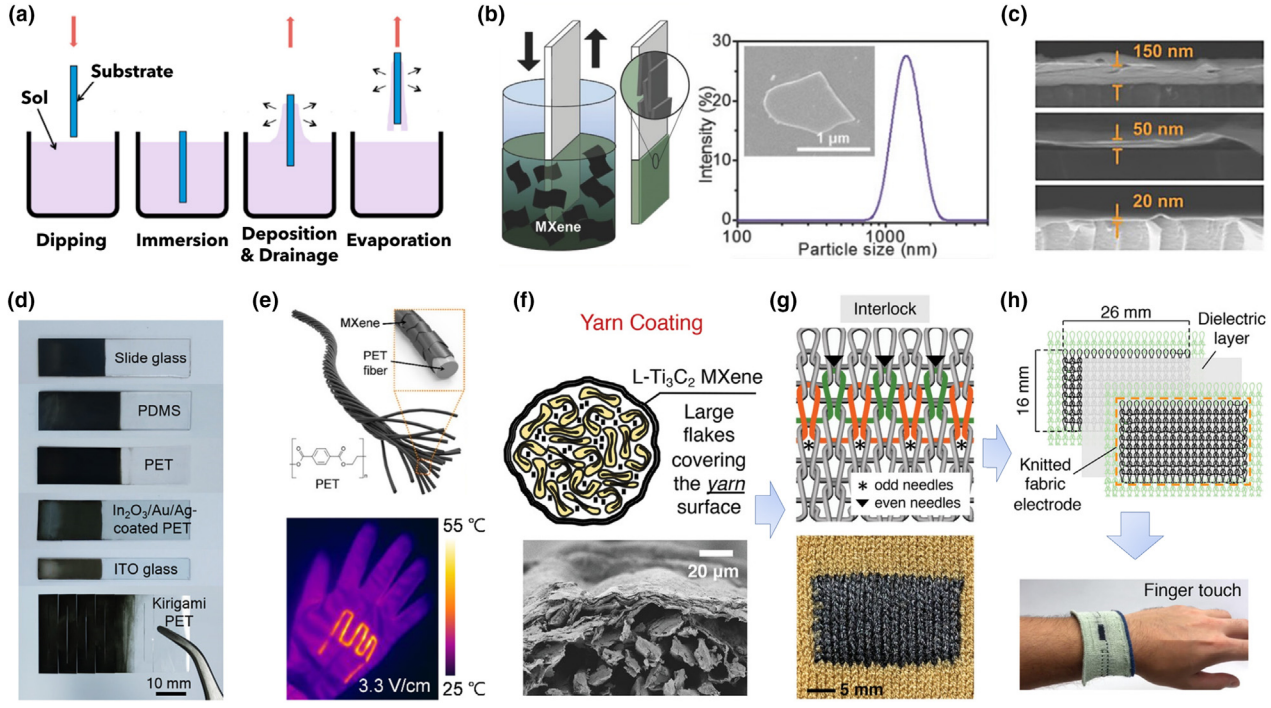

FIGURE 10

Dip-coating of MXene dispersions. (a) Dip-coating steps to fabricate thin films. Reproduced from ref. [216] with permission from MDPI. (b) Schematic image of optically transparent $Ti_3C_2T_x$ MXene film prepared by dip-coating (left), flake size distribution (right) of MXene dispersion. (c) Cross-sectional SEM images of dip-coated MXene films on glass substrates. Reproduced from ref. [151] with permission from Wiley-VCH. (d) Optical images of dip-coated MXene-PDAC films. Reproduced from ref. [152] with permission from AAAS. (e) Schematic image of a PET fiber coated with MXene flakes (top) and the corresponding IR image of the cotton glove sewed with MXene threads (bottom). Reproduced from ref. [153] with permission from American Chemical Society. (f) Schematic image of the cross-sectional of cotton yarn coated with MXene flakes (top) and corresponding cross-sectional SEM image (bottom). (g) MXene dip-coated cotton yarn knitted with interlock stitch pattern. (h) Assembly of capacitive knitted pressure sensor based on MXene dip-coated and knitted fabric electrodes with scheme (top) and read device (bottom). Reproduced from ref. [154] with permission from Wiley-VCH.

flakes, providing a strong adhesion on the as-obtained yarn electrodes. It is worth mentioning that for these porous, lightweight, cellulose substrates, the abovementioned processing techniques such as inkjet printing, aerosol jet printing, and screen-printing are not suitable due to the uneven distribution of flakes upon deposition; only the substrate surface are utilized while plenty of internal fibers are left as blank. On the other hand, the dip-coating strategy is particularly suitable for these porous cellulose substrates to produce MXene-based yarn electrodes. By designing stitch patterns, these MXene-yarn electrodes can be further knitted into smart textiles (with half-gauge and interlock patterns, Fig. 10g) for pressurized sensor applications (Fig. 10h) [154].

Similar to previous fabrication techniques, these dip-coated MXene thin films can also be employed as microsupercapacitors for energy storage, yet features a high optical transmittance, up to 98% at 550 nm, due to the intrinsic low optical absorption properties of MXene [151]. Interestingly, it is recently revealed that a dip-coated MXene film can functions as both a transparent conductive electrode and an electrochromic device. The absorption peaks can shift from 770 to 670 nm, due to the protonation/deprotonation process of oxide-like surface functionalities on MXene [155].

Spray-coating

When the viscosity of MXene dispersion is relatively low, direct spraying of the colloidal dispersion allows for the fabrication of large-area MXene films for the quick examination of materials/devices properties, as guided by Fig. 6. Up to now, delaminated MXene aqueous dispersions are typically utilized for spray-coating in order to give conductive thin films; Except for ethanol-based colloidal solution [139], reports on non-aqueous MXene dispersions are quite limited. This is because non-aqueous solvents that are able to disperse MXene flakes are limited to polar organic media whose Hildebrand and Hansen parameters match well with those of MXenes [117]. While dispersing the flakes well, the majority of these polar organic solvents possess a high boiling point, leading to the difficulty in evaporating the solvent at low temperature thus limiting the film thickness and procedure efficiency. This is schematically demonstrated in Fig. 11a. In general, delaminated MXene aqueous dispersion with concentration ranging from 0.1 mg/mL to 10 mg/mL are suitable for spray-coating. It is worth noting that even under similar solid fraction, delaminated flakes dispersion possesses higher viscosity compared to that of multilayered MXene suspension [137], rendering their solution processing methods different.

Typically, MXene dispersions loaded in the spray gun are ejected by the high-pressure carrier gas in the form of aerosol droplets. The velocity and diameter size of the droplet are controlled by the gas pressure. Once ejected and deposited on hot substrates, the droplets merge and are subjected to solvent evaporation, leaving dried flakes aligned in parallel to the substrate. Through the movement of the spray-gun in the X-Y direction, the percolative network starts to form and thus continuous MXene thin films/coatings are achieved. In other words, spray coating allows fast fabrication of large-area thin films (from nm to μm range). Uniformity of the resultant MXene films is governed by parameters such as solvent type, velocity, the distance between substrate and nozzle, temperature, etc. [156]. Through optimizing the substrates' surface (i.e. plasma treatment, etching the surface oxide layer, etc.), the as-deposited MXene film can be strongly attached to the substrates without peeling-off, even under repeated deformation such as bending.

Due to the excellent electrical and mechanical properties in the delaminated MXene nanosheets, the sprayed MXene film can be employed as electrical contacts (i.e. gate, source, and drain) for thin-film transistors (Fig. 11b) [82], current collectors (Fig. 11c) [160], bottom electrodes for triboelectronic nanogenerators (Fig. 11d) [161], mechanical reinforcements (Fig. 11e) [162], transparent conductive electrodes [139], etc.

Of particular attention is the applications of the sprayed MXene thin films in wireless communication, as shown in Fig. 11f. It is revealed that the reflection coefficient is MXene thickness-dependent; thicker films generally give higher reflection coefficient and lower attenuation (Fig. 11f) [163]. As MXenes provide the highest conductivity, as well as water-dispersible, among other solution-processed 2D materials, direct spraying of MXene dispersions holds great promises for scalable manufacturing of radio-frequency antennas. On the other hand, through the spray coating technique, microsupercapacitors can be easily fabricated by template masking [157], scalpel engraving [151], laser scribing [158–160], etc. It is worth mentioning that these fabrication routes only produce symmetric microsupercapacitors, with the electrode thickness depending on the spray coating conditions as explained above. Due to the excellent electrical and charge storage properties of MXenes, the spray-coated MXene films not only function as the current collector, but also active material, eliminating the necessity of bulky metal foils to transport electrons. As a result, spray-coated MXene microsupercapacitor generally showcase excellent power handling and good capacitance, as seen in Fig. 11g [157].

Spin-coating

As increasing the viscosity of MXene dispersions to the medium range (10∼200 mPa·s) or medium concentration range (1∼20 mg/mL), then spin coating is recommended to process MXene dispersions (Fig. 6). The spin-coating technique is the most well-known solution-processing method to produce thin, uniform films from dispersions. In general, the dispersion first wets the substrate, and the liquid layer starts to spread over the substrate upon rotation. As spinning continues, the majority of the dispersion flies off, leaving a thin liquid layer behind on the substrate and enabling a fast solvent evaporation rate. Consequently, homogeneous thin films are achieved (Fig. 12a) whose thickness depends on MXene concentration, spin speed, duration, etc. For instance, Spin-coating of MXene dispersion with a higher concentration (i.e. >10 mg/mL) results in films that are thicker compared to that of more diluted dispersion (i.e. ∼1 mg/mL) at a given spin speed [139]. Typically, films with thickness ranging from nm to μm and various transmittances can be simply obtained through spin-coating technique, thus is particularly suitable for lab-scale prototype devices with a flat substrate surface.

Indeed, spin-coated films possess better flake alignment compared to films fabricated by other methods. This is largely attributed to the centrifugal force applied on the liquid layer, forcing

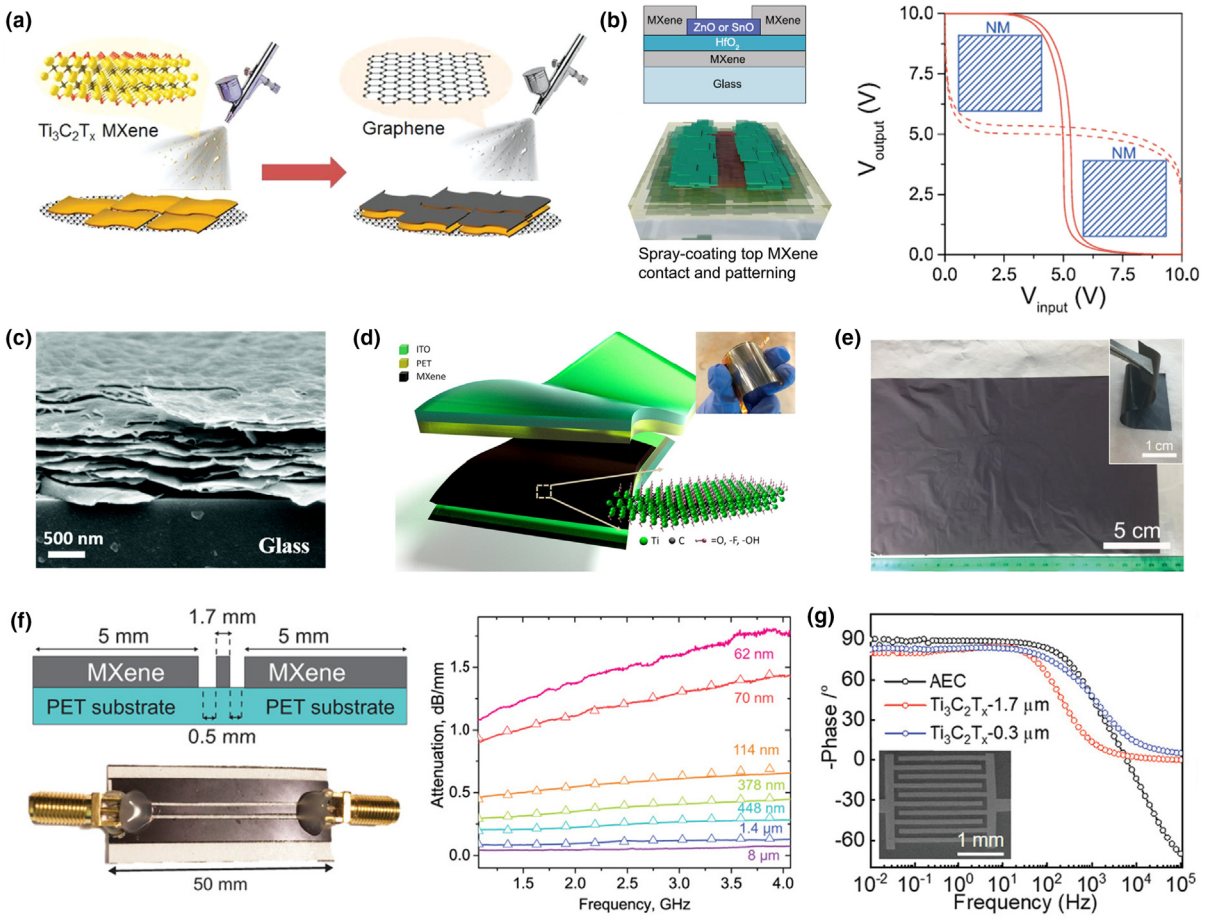

FIGURE 11

Spray-coating of MXene dispersions. (a) Schematic demonstration of boiling point effect on the resultant film morphology and quality. (b) Spray-coating of top MXene contacts and patterning of TFT devices with all-MXene contacts (left) and noise margin extraction from the butterfly plot (right). Reproduced from ref. [82] with permission from Wiley-VCH. As-sprayed MXene films as (c) current collector, (d) bottom electrode for the TENG, (e) mechanical reinforcement, (f) wireless communication with schematic and digital photo of the MXene CPW TLs (left) and attenuation vs thickness (right). Reproduced from ref. [160–163] with permission from Royal Society of Chemistry, Elsevier, Wiley-VCH, AAAS, respectively. (g) Bode phase angle plots of $Ti_3C_2T_x$ MXene film-based microsupercapacitor prepared by spray-coating. Reproduced from ref. [157] with permission from Wiley-VCH.

the suspended nanosheets to comply and align in parallel to the direction of outward centrifugal force in order to minimize the free energy. As shown in Fig. 12b, the spin-coated MXene flakes are compactly aligned and lie flat on the substrate without wrinkles or porosity [76], the latter morphology typically found in the spray-coated MXene films [164]. The highly aligned nature of the flakes after spinning is further evidenced by the strongest (0 0 2) peak among other (0 0 *l*) peaks in the X-ray diffraction pattern, as well as the higher intensity of (0 0 2) peak in the spin-coated sample than that of spray-coated one (Fig. 12c) [78]. The ordered alignment of flakes results in an improved transport of charge carriers among the interflake junctions, leading to higher electrical conductivity, lower contact resistance/sheet resistance, and smaller surface roughness in the resultant spin-coated MXene films.

Benefited from such an aligned architecture, spin-coated MXene films have demonstrated quite promising performances in prototype thin films/devices such as perovskite solar cells [165], field-effect transistors (FET) [166], transparent conductive electrodes (TCEs) [78], light-emitting diodes (LEDs) [167], supercapacitors [26,76], etc. Particular attention has been paid to the fabrication of microsupercapacitors assisted by laser scribing strategy (Fig. 12d) [168], where interdigitated electrode fingers are easily formed on a wafer-scale substrate. By decreasing the MXene concentration or increasing the spin speed, the film thickness can be effectively reduced to the nanoscale, resulting in highly transparent conductive MXene films [75,78]. These spin-coated transparent films exhibit excellent bulk conductivity without percolation problems [76], thus can be used for the electrical contacts in various optoelectronic devices. For instance, organic FETs based on spin-coated MXene doped with NH_3 showcase a maximum carrier mobility of $\sim 1\ cm^2 \cdot V^{-1} \cdot s^{-1}$ and an on–off current ratio of $\sim 10^7$ (Fig. 12e) [169].

On the other hand, through chemical modification of the spin-coated MXene films surface with a conducting polymer hole-injection layer, high quantum-efficiency (~28.5% ph/el), flexible organic LEDs are thus engineered (Fig. 12f) [167]. Beyond that, the spin-coated MXenes have also demonstrated a great potential for replacing gold in GaAs photodetectors, since the former exhibits significantly higher responsivities and quantum

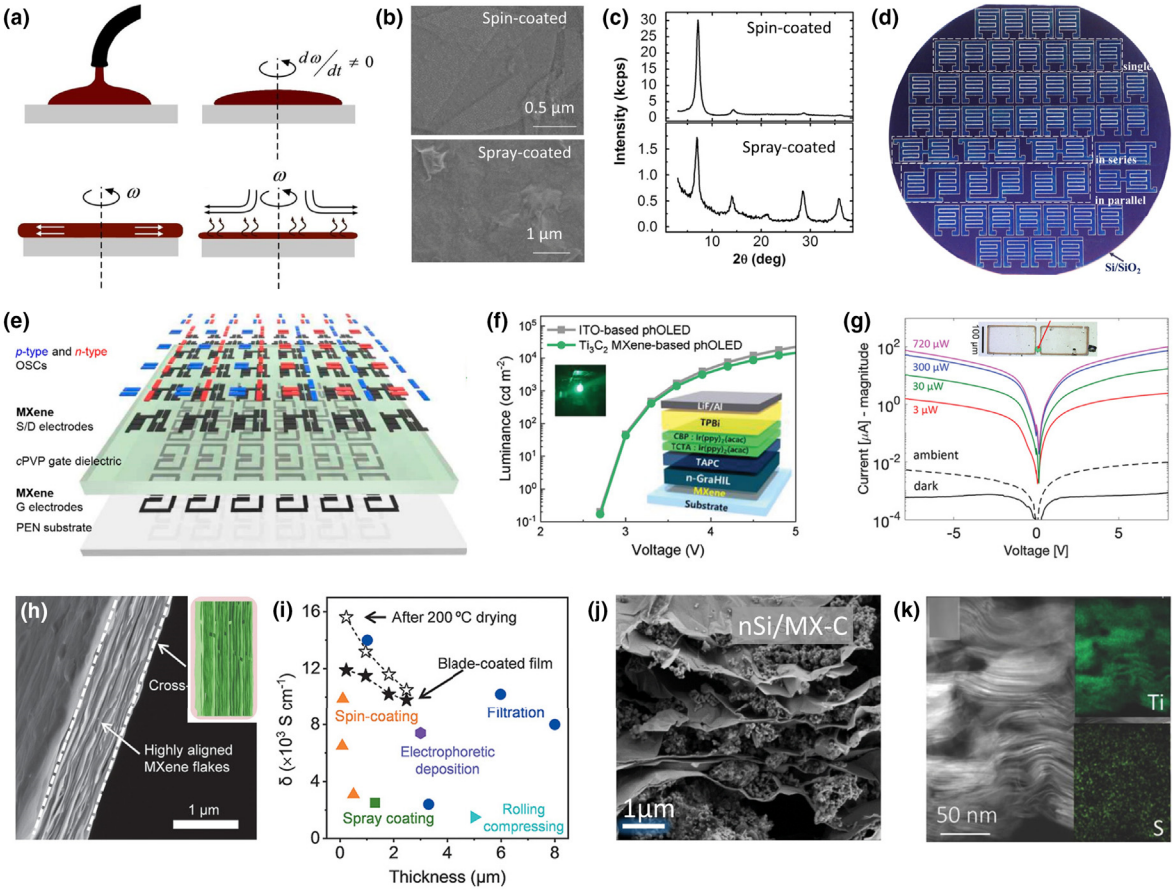

FIGURE 12

Spin- and blade-coating of MXene dispersions. (a) Scheme of spin-coating steps. (b) SEM images of spin coated (top) and spray coated (bottom) MXene films with their corresponding XRD patterns shown in (c). Reproduced from ref. [76,78] with permission from Wiley-VCH. (d) Digital image of MXene-based on-chip MSCs. Reproduced from ref. [168] with permission from Elsevier. (e) Scheme image of OFET device based on spin-coated MXene electrodes. Reproduced from ref. [169] with permission from American Chemical Society. (f) Luminance plotted as a function of voltage of OLEDs based on ITO and spin-coated MXene electrode, respectively (insets are OLED device (left) and device structure (right)). (g) Current-voltage profile of photodetector based on spin-coated MXene electrode at 532 nm with inset being the confocal microscopy image of the real photodetector device. Reproduced from ref.[167,170] with permission from Wiley-VCH. (h) Cross-sectional SEM image of blad coated MXene films (inset shows the aligned flakes). (i) Electrical conductivity comparison for MXene films through different processing methods. Reproduced from ref. [21] with permission from Wiley-VCH. (j). Cross-sectional SEM image of MXene-Si blade-coated films. Reproduced from ref. [172] with permission from Nature Publishing Group. (k) Cross-sectional TEM image (left) coupled with elemental mapping of Ti (top right) and S (bottom right) of blade-coated MXene-S films. Reproduced from ref. [179] with permission from Wiley-VCH.

efficiencies under similar dark currents (Fig. 12g) [170], implying wide potential applications in low-cost flexible optoelectronic devices. In addition to energy- and optical-related devices, the 2D compacted and confined space in the spin-coated MXene films also facilitate potential applications for nanofluidics (i.e. molecular sieving, gas separation, and transportation) [171].

Blade-coating

Another solution-processing technique for large-scale production of MXene films is blade-coating, the technique that suits MXene dispersions with a higher concentration (20∼200 mg/mL) or viscosity (up to 2000 mPa·s), as shown in Fig. 6. Similar to spin-coating, blade-coating of concentrated MXene dispersions results in large-area freestanding MXene films with highly oriented flakes, leading to excellent electrical conductivity and mechanical properties (such as tensile strength, Young's modulus). Blade-coating typically gives μm-thickness MXene films depending on the blade height and MXene concentration. It is known that delaminated, concentrated MXene dispersions (i.e. apparent viscosity > 1 Pa·s) exhibit a rheological shear-thinning behavior, enabling good flowability and processability [172]. Diluted dispersions with a low concentration (<10 mg/mL), however, tend to spread over the substrate since the viscosity is relatively low, thus is not suitable for blade-coating. Blading viscous MXene inks creates the shear force that drives MXene flakes to align along the direction of velocity. In addition, dispersions with higher elastic (G') and viscous (G'') moduli and a high G'/G'' ratio are preferred, which are beneficial for recovering to the gel state and maintaining the flake alignment once the shear force is removed [21]. Upon solvent evaporation, large-area conductive MXene films are thus achieved.

Importantly, pre-selection of MAX particle size has been proven effective to produce MXene flakes with larger lateral size, leading to a higher orientation factor value (0.75) thus increased

anisotropy compared to that of the self-assembled film (i.e. filtration method, orientation factor of 0.64), as well as compacted film morphology without plenty of voids, as shown in Fig. 12h [21]. Consequently, the blade-coated MXene film (thickness ~ 214 nm) demonstrates the highest conductivity up to 15,100 S/cm, greatly surpassing those of spray- and spin-coated MXene films under similar film thickness (Fig. 12i) [21]. When blade-coating delaminated/multilayered MXene mixed slurries, the film surface uniformity is greatly compromised due to undesirable flake alignment, thus inevitably results in inferior conductivity [173].

Indeed, the blade-coating technique has been widely applied in battery electrodes fabrication [174–176]. For most MXene-based rechargeable battery anodes, multilayered MXenes were utilized for blade coating [177,178]. These multilayered particles function either as active materials for accommodating Li^+ or hosts for guest active species to store Li^+. By employing delaminated MXene nanosheets as conductive binders through forming an interconnected network with active materials such as Si, S by a simple blade-coating of MXene-active material mixtures, large-area battery electrodes can be manufactured. For example, the blade-coating MXene-Si mixture results in quite thick electrodes (up to 450 μm) with the aligned flakes providing good mechanical reinforcement as well as conductivity (Fig. 12j) [172]. On the other hand, blade-coating MXene-S inks lead to large-area, conductive, robust cathode with highly densified stacking of MXene flakes (Fig. 12k), which have shown excellent rate performance and ultralow capacity decay rate in Li-S battery [179]. It is worth noting that the alignment of MXene flakes would be disrupted once the thickness increase beyond a critical threshold after drying, introducing voids and weak interflake interactions, thus compromising the electrical and mechanical properties [21]. In other words, thick, super-strong, and conductive MXene films by blade-coating technique are still yet to develop and should be the next research focus regarding this processing method.

Interfacial assembling

Interfacial assembling allows the assembly of MXene nanosheets with nanoscale thickness. Due to negative charge groups such as –OH, –F, and –O groups terminated on the MXene surface, electrostatic repulsive force suspends delaminated MXene flakes homogeneously in water. Through mixing with another type of dispersion with a positive zeta potential, the negative surface charges on MXene flakes are screened, leading to flocculation and consequently the formation of hybrids (Fig. 13a) [77,180]. Polymers, metal oxides, and other guest species (CNTs, graphene oxides, silicon carbide nanowires, etc) can be chemically modified to render their surface positively charged [181–183]. Composites such as MXene/CNTs [180], poly (diallyldimethylammonium chloride)/MXene [184], MXene/polystyrene [77], and other hybrids [183] can be effectively obtained through such an interfacial assembly technique. In addition, the interfacial assembling is useful for the fabrication of conformal coatings and nanoscale control over the entire layered film thickness due to the self-limiting nature of the electrostatic adsorption [185,186]. Nevertheless, this method lacks scale-up possibility with film thickness typically limited within μm. Thicker films can also be prepared by combining interfacial assembling with other processing methods such as blade-coating or vacuum-assisted filtration. Besides relying on electrostatic adsorption to perform the assembly process, engineering the surface functionalities on the guest species (i.e. polymers) also turns out effective. For instance, MXene flakes tend to spontaneously wrap poly(methyl methacrylate) (PMMA) spheres due to the hydroxyl surface groups on the latter through hydrogen-bonding [187]. By vacuum-filtrating the MXene/PMMA mixtures followed by annealing, a 3D macroporous film consisted of hollow MXene spheres was obtained (Fig. 13b), which showcased excellent Na-ion storage capacity [187].

Of particular attention is the formation of MXene-based heterostructures. Through polymerization of resin/block copolymer micelles on MXene substrate (where cross-linking occurs), mesostructured nanosheets can be achieved with uniform porosity and a sandwiched morphology (Fig. 13c) [188], being an ideal host for S for achieving high-performance Li-S battery cathode after removing the F127 [188,189]. In addition, hydrothermal assembly is also effective in constructing MXene-based heterostructures, such as rGO/MXene aerogels [190], carbon-$MoSe_2$/MXene (Fig. 13d, where the delaminated MXene flakes are used as conductive substrate and anchor the $MoSe_2$ seeds through strong covalent bonds, similar as Fig. 13c) [191], TiO_2/MXene [192], etc., despite that MXenes are likely to be oxidized under the hydrothermal condition. Aside from these energy-intensive strategies, and also to avoid potential degradation of MXenes, van der Waals (vdW) assembly triggers non-harmful, spontaneous formation of metal oxides/MXene micelle-like heterostructures at the interface of MXene-poor solvent such as tetrahydrofuran [193]. The vdW assembly technique opens vast opportunities for constructing a range of high-performance heterostructured hybrids at room temperature, rendering great potential applications in fields like energy storage, catalysis, sensing, etc.

Beyond assembling of MXene-guest species hybrids, spontaneous assembly of MXene thin films is also possible at the liquid–air interface [194] or liquid–liquid interface [129,195,196]. MXene flakes tend to undergo direct assembly of 2 nm monolayer-thick films at the liquid–air interface at pH ~ 8, while in the acidic medium, anion coordination of MXene flakes is triggered with the formation of anion/MXene/subphase interface, and finally assembled into dense monolayer films by layer compression with a surface pressure ~40 mN/m [194]. As of liquid–liquid interfacial assembly, typically a second organic solvent is required to create a water–oil interface. Based on that, adding organic acid ligands (such as alkylphosphonic acid) is able to drag MXene flakes from the water phase to the oil phase due to the formation of a covalent Ti-O-P bond by an interfacial nucleophilic and sequential condensation reaction [129]. Another example is that adding aminefunctionalized polyhedral oligomeric silsesquioxane (POSS-NH_2) to toluene is able to significantly reduce the water-toluene interfacial tension. This facilitates the cooperative assembly of MXene nanosheets and POSS-NH_2 in the interface, leading to the assembly of MXene-surfactant robust film that possessing a hydrophobic tail when jammed (Fig. 13e and f) [197]. Similarly, when adding n-butylamine to MXene aqueous dispersion-toluene mixture, MXene nanosheet surfactant is formed and jammed at the inter-

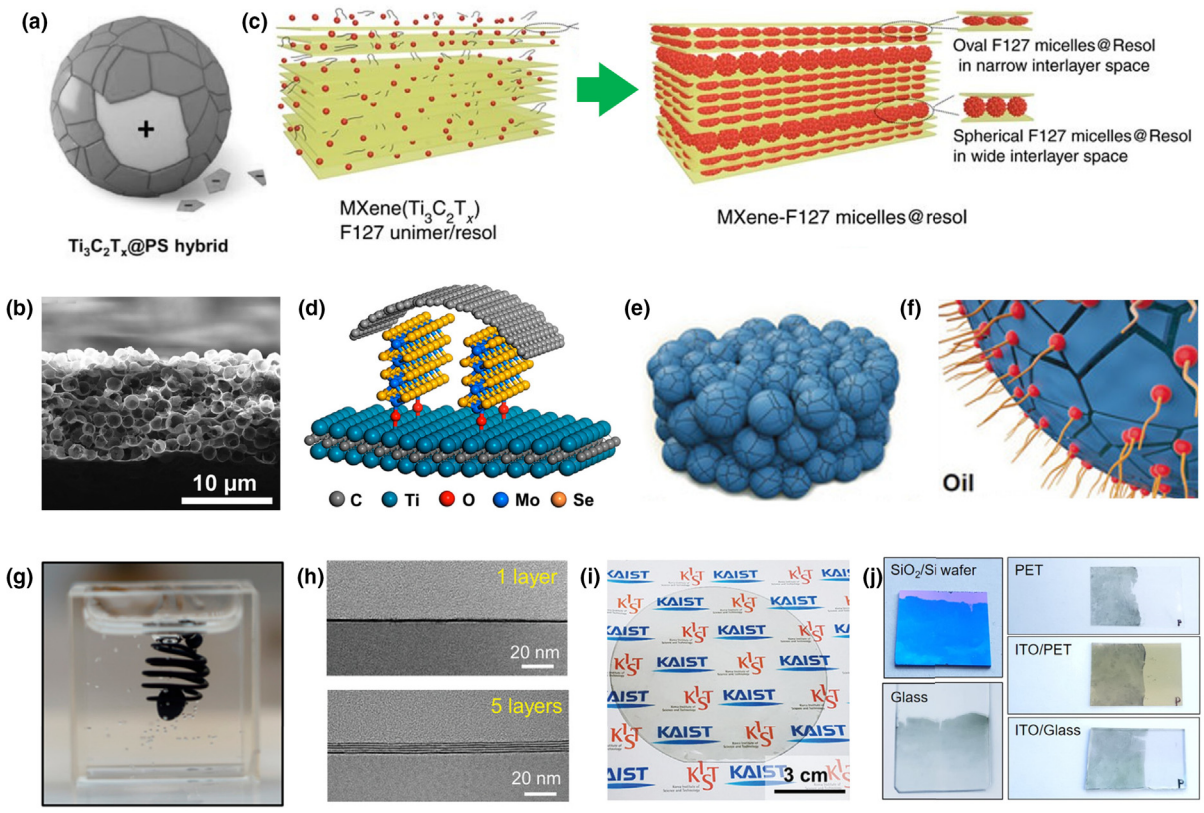

FIGURE 13

Interfacial assembly of MXenes. (a) Scheme of assembly of $Ti_3C_2T_x$ MXene nanosheets on polystyrene spheres (PS) based on electrostatic interaction. Reproduced from ref. [77] with permission from Wiley-VCH. (b) Cross-sectional SEM image of 3D macroporous MXene film consisted of hollow MXene spheres. Reproduced from ref. [187] with permission from Wiley-VCH. (c) Scheme of MXene-F127 micelles@resol composite. Reproduced from ref. [188] with permission from Nature Publishing Group. (d) Scheme of MXene/$MoSe_2$/carbon heterostructure. Reproduced from ref. [217] with permission from American Chemical Society. (e and f) Scheme of pickering emulsions and MXene aerogels by using MXene surfactants. Reproduced from ref. [197] with permission from Wiley-VCH. (g) Printing of sculpted structure in silicone oil based on MXene-ligand surfactant. Reproduced from ref. [195] with permission from American Chemical Society. (h and i) Cross-sectional TEM images of monolayer and 5-layer assembled MXene films, respectively (left) and as-assembled MXene transparent conductive films (right). Reproduced from ref. [196] with permission from Wiley-VCH. (j) Optical images of interfacial-assembled MXene films transferred to various planar substrates using the static transfer method. Reproduced from ref. [198] with permission from American Chemical Society.

face, resulting in 3D sculpted liquids that enabling further processing such as all-liquid printing (Fig. 13g) [195].

On the other hand, densely packed, ultrathin MXene films can be assembled by the strong vertical convection induced by the evaporation of ethyl acetate, as well as the Marangoni effect derived from the surface tension difference between water and ethyl acetate [196]. The interfacial assembled film is of atomic-level precision with thickness well-controlled (Fig. 13h) and forming highly transparent and conductive films (Fig. 13i) [196]. When hydrochloric acid is added to the above MXene-water/ethyl acetate mixture, the interflake electrostatic repulsion is minimized due to higher zeta potential, resulting in films that strongly adhering to various substrates, including curved structures (Fig. 13j) [198].

Vacuum-assisted filtration

Vacuum-assisted filtration is one of the most common routes to fabricate thin films with thicknesses ranging from nanoscale to microscale. Typically, this process involves MXene dispersions and commercial filtering membranes such as cellulose ester or polypropylene membrane (Celgard 3501, separator) and a vacuum-generated setup. The pore size of the filtering membrane is critical for trapping MXenes particularly for nanosheets with small lateral flake size. As MXene aqueous dispersion is filtered through the ester membrane, for example, water is able to pass through the pores while MXene flakes are trapped above the membrane. The filtration rate is governed by the accumulation of MXene flakes above the pores. Therefore, as the number of MXene flakes increases at a given location on the filter paper, the filtration speed decreases but does so to a lesser degree at thinner or uncovered regions. As such, the filtration process is intrinsically self-regulating [199], allowing the fabrication of uniform MXene films with reasonably even thickness. By simply varying the concentration of MXene dispersions, and/or filtrating volume, MXene films with different thicknesses can be thus achieved on the filter paper. While filtrating on hydrophilic Celgard 3501 membrane enables automatic peeling-off of MXene films after the paste gets dried naturally, films filtered on cellulose ester need to be transferred to target substrates by dissolving the membrane (i.e. immersing in acetone). We note that despite MXene films may be transferred by this method, possible wrinkles or damages may occur on the films after transferring. In

addition, incomplete dissolution of the filter paper may also compromise the film quality, limiting the vacuum-filtration/transfer plausibility when high-quality MXene films are desired.

Prior to vacuum filtration, MXene inks should be diluted to the state that apparently flowable; too much viscous inks are not suitable for vacuum filtration since non-uniform films would thus form. In addition, dispersions with very high concentrations greatly extend the filtration time to complete the process, exposing MXene flakes to ambient conditions thus resulting in MXene degradation. However, as stated previously, the filtrating speed gradually becomes slow as the process continues, therefore, excess volume inevitably leads to almost "static" filtration once the flakes are assembled into a compact film with much sluggish water transport kinetics. In other words, the thickness of MXene filtrated film is typically limited to several μm. Thicker MXene films can be achieved through other techniques such as blade-coating mentioned above.

Apart from film thickness, the flake alignment in the filtrated film is not as orientated or compact as that of blade-coated film, the latter creates a strong shear effect to force the flakes to align. Instead, after vacuum filtration, MXene flakes stacked due to van der Waals force and possess wrinkled, loosely packed sheets (Fig. 14a), leading to a specific surface area of 22.6 m^2/g in a vacuum-filtrated MXene freestanding film (Fig. 14b) [200]. As such, the filtrated MXene membrane provides ideal channels for nanofluidic transport with ionic conductivity 1–2 orders of magnitude higher than that of bulk electrolyte (Fig. 14c) [201]. When the filtrated film is immersed in 3 M H_2SO_4 electrolyte, the resultant MXene hydrogel films showcase very high rate-handling properties (pseudocapacitive response maintained at 100 V/s), due to the fast nanofluidic transport behavior within the nanochannels, as well as high accessibility of protons to the deeper redox-active sites (Fig. 14d) [202]. While hydrophilic MXene films are preferential for the nanofluidic devices, other applications such as waste oil removal, require hydrophobic, lightweight foam. To this end, filtrated MXene films can be switched to hydrophobic, lightweight foam through annealing in hydrazine, which selectively reduces and gasifies the oxygen-containing surface groups on MXene (Fig. 14e) [203].

In addition to filtrate pure MXene dispersion, filtrating blend suspensions or alternative filtration result in MXene-based hybrid films that possessing properties from both components, i.e. high conductivity, good mechanical flexibility, and high capacitance, etc. MXene/CNT (Fig. 14f) [204], $Fe(OH)_3$/MXene [205], Co_3O_4/MXene [206], polymer/MXene [102], and other related composite films can be similarly fabricated through vacuum filtration. For instance, when filtrating polyvinyl alcohol (PVA) and MXene blend suspension, PVA molecules are well intercalated within MXene flakes (Fig. 14g), resulting in much enhanced mechanical properties while still being conductive as long as MXene content is higher than 10 wt.% [102]. It is worth mentioning that the as-filtrated hydroxides/MXene and oxides/MXene hybrid films can be used to create MXene membranes with short transport pathways, by etching away hydroxides and oxides, respectively [205]. These unique MXene or MXene-based membrane thus open vast opportunities for applications ranging from water purification, energy storage, sensing, catalysis, and so on [25,30,207].

Other techniques

Besides processing techniques discussed above, other approaches such as Meyer rod coating [173], stamping and painting [208], patterning [209], etc. are also emerging for solution-processing MXene dispersions. Meyer rod coating involves viscous MXene pastes which is spread by a Meyer rod on the substrate [173]. Substrates should be hydrophilic regardless of porous (i.e. paper, textiles) or non-porous (i.e. glass, metal foil). This method works fundamentally based on the shear force created upon the rod movement, which is similar to that of the blade-coating technique. However, coatings produced by Meyer rod typically possess a much rougher film surface and less even thin thickness [173]. Moreover, these viscous MXene pastes can be used as clay for stamping assisted by 3D printed stamps, enabling quick fabrication of various functional devices/patterns, such as micro-supercapacitors (Fig. 14h) [208]. On the other hand, by printing patterns as a template prior to vacuum-assisted filtration of MXene dispersions, planar symmetric micro-supercapacitors can be achieved after sputtering and lift-off processes [209].

It is also worth mentioning that when coming to real practical devices such as micro-supercapacitors, techniques with a low fabrication cost and a high compatibility to current industrial facilities while showcasing high device-level performance, are highly desired. To this end, developing new approaches is of significance to push MXene towards real-world and practical applications. For example, direct writing of aqueous MXene ink enables simple but efficient fabrication of conductive tracks, and micro-supercapacitors for electronics and electrochemical energy storage, respectively (Fig. 14i) [210]. Functional MXene-based fibers with enhanced electrical and mechanical properties is another instance, which is realized by electrospinning of MXene dispersions [211]. Apart from these methods, freeze-drying MXene dispersions also allow the preparation of few-layered MXene powders with minimal flake restacking [176,212,213]. In particular, by adding high-aspect-ratio nanomaterials (carbon nanotubes, graphene, cellulose nanofibrils, etc.) into MXene dispersion followed by freeze-drying, ultralight MXene-based aerogels and sponges can be fabricated with high electrical conductivity (Fig. 14j). These lightweight aerogels have showcased excellent performances in strain sensing [214], energy storage [215], electromagnetic interference shielding [29], etc.

Summary and perspectives

MXenes are a new and fast-growing class of 2D materials, exhibiting plenty of exotic properties and enabling numerous promising applications. Cutting-edge technologies and high-performance devices require efficient processing of MXene colloidal dispersions into films/structures. This highlights the significance of the solution processing and formulation of functional MXene inks. Of the same importance is the understanding of the colloidal and rheological properties and methods to tune the flow behavior of the inks, their wetting (and adhesion), drying kinetics, etc. In other words, mastering the basics of the solution processing is necessary for the proper selection of a processing method and systematic optimization of the process parameters, which is a vital requirement for the successful utilization of the MXenes in different applications.

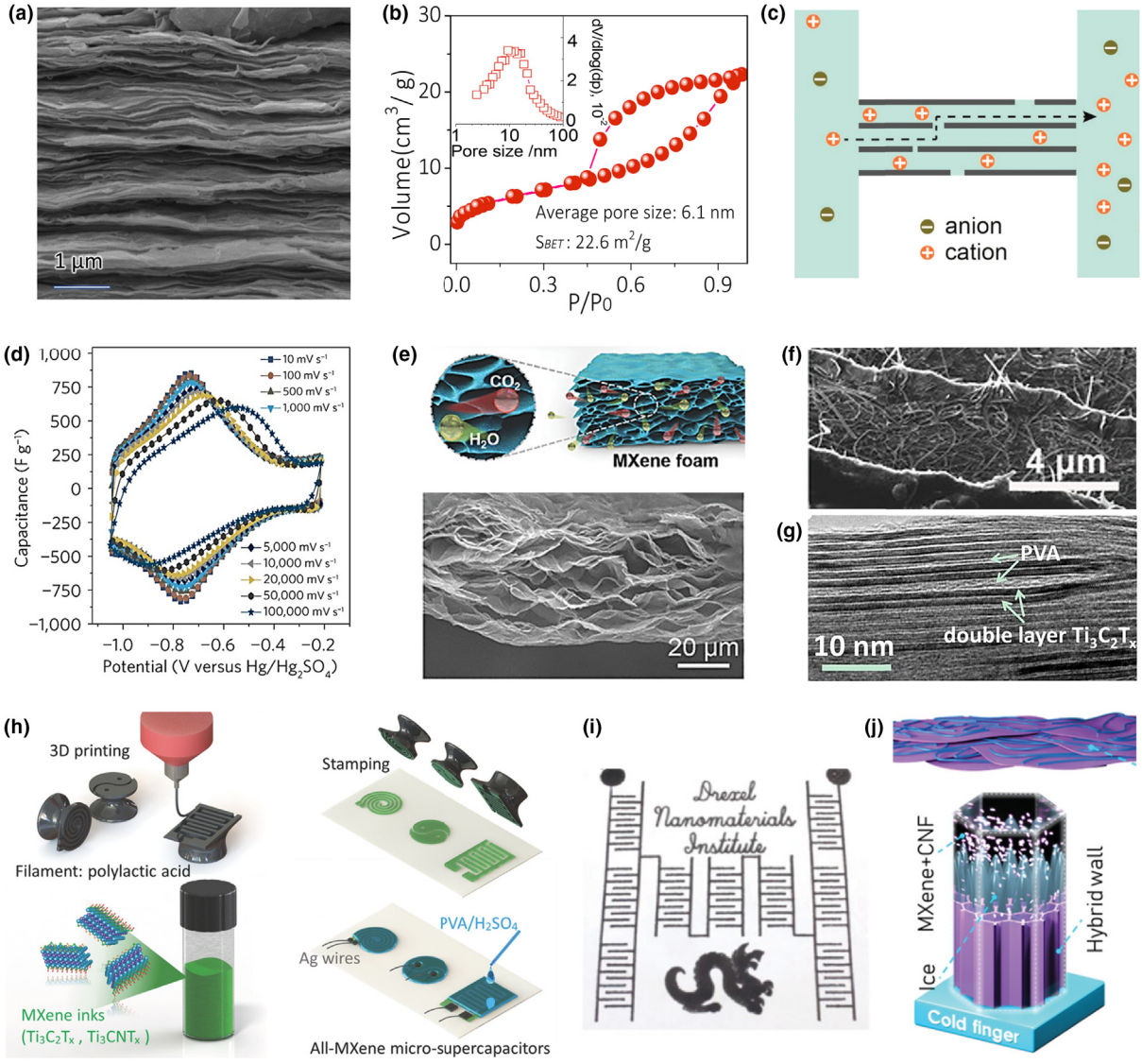

FIGURE 14

Vacuum filtration of MXene dispersions and other emerging techniques. (a) Cross-sectional SEM image of a pure filtrated MXene film and its N_2 adsorption/desorption isotherms in (b) with inset showing the pore size distribution. Reproduced from ref. [200] with permission from Wiley-VCH. (c) Scheme of MXene filtrated film for water transport within the nanochannels. Reproduced from ref. [201] with permission from American Chemical Society. (d) Cyclic voltrammograms of a filtrated MXene hydrogel film under various scan rate. Reproduced from ref. [202] with permission from Nature Publishing Group. (e) Scheme of formation of the MXene foam (top) and its corresponding cross-sectional SEM image (bottom). Reproduced from ref. [203] with permission from Wiley-VCH. (f) SEM image of a filtrated MXene/CNT film. Reproduced from ref. [204] with permission from Wiley-VCH. (g) Cross-sectional TEM image of a PVA/MXene filtrated film. Reproduced from ref. [102] with permission from National Academy of Sciences of the United States of America. (h) Scheme of stamping of micro-supercapacitor patterns based on 3D printed stamps and MXene viscous inks. Reproduced from ref. [208] with permission from Wiley-VCH. (i) Direct written pattern using a homemade pen filled with MXene dispersions. Reproduced from ref. [210] with permission from Wiley-VCH. (j) Scheme of MXene/cellulose nanofabrils aerogel achieved through unidirectional freezing process of the mixed dispersion. Reproduced from ref. [29] with permission from Wiley-VCH.

As such, here in this contribution, we have reviewed the solution processing strategies for colloidal MXene dispersions in detail. In particular, we have proposed a "map of guidelines" for solution-based processing. This map allows the efficient processing of MXenes into high-performance devices by considering the throughput and important figures of merit. These processing guidelines can be beneficial to both MXene beginners or expert researchers working on other topics, who wish to set their foot in this booming investigation field.

Indeed, we believe the physicochemical properties of MXenes have profound effects on the solution processing. For example, delaminated MXenes with larger lateral size and/or oxygen-containing terminated groups possess a lower viscosity at a giving solid content in the colloidal solution, which impacts the ink formulation. Therefore, to unveil such influences and achieve more efficient solution processing of MXenes, we believe future efforts should be dedicated to the following:

(1) Expanding the understanding of their basic physicochemical properties and manipulating these properties through either physical or chemical strategies. In particular, revealing the impact of MXene surface modifications on the bandgap, electrical conductivity, work function, magnetism, superconductivity, etc., and determining these impacts in different MXenes coupled with different M, X, should be investigated in more depth. The surface engineering brings changes to MXenes' hydrophilicity, ink formulations, and thus rheological properties, which further influence the processing methods. In other words, the flow behavior of surface-modified MXenes should be conducted, based on which suitable processing routes can be determined.

(2) From a broader perspective, scalable processing is required to turn MXenes into real products. This means that MXenes should be etched and delaminated in large quantities, instead of several grams on the lab-scale. New etching/delamination methods are strongly needed with minimal impact on the environment. Recently, manufacturing 50 g multilayered MXenes have been reported [212]. However, scalable production of MXenes is associated with another critical issue – oxidation stability of delaminated MXene dispersions. Measures to extend the shelf life of MXene aqueous dispersions in the absence of additional chemicals are more preferred.

(3) Finally, for scalable printing and coating of MXenes on different industrially-important substrates (e.g. polyethylene terephthalate, PET) with high resolution, MXene ink formulations require more research attention. As screen printing or aerosol-jet printing requires inks completely different from inkjet printing (according to the map in Fig. 6), one cannot easily convert an inkjet-printable ink to a screen printing or other printing methods ink. As such, developing suitable ink formulations for individual printing techniques and each MXene is of great importance. For example, upon screen printing, drag-out inks from the substrate is typically observed, which is due to the high elasticity of the MXene inks, compromising the quality of printed lines. Developing suitable ink formulations and subsequently printing high-resolution lines (that is, uniform yet narrow line-width along the axial direction) and smooth surface (that is, a small surface roughness) are of great importance, which can revolutionize MXene-based electronics, such as miniaturized energy storage, electromagnetic interference shielding, radio-frequency identification, wearable sensors, to name just a few.

Author contributions

Conceptualization: C.F.Z., H.Z.
Data curation: C.F.Z., S.A., X.T.J.
Formal analysis: S.A., C.F.Z., X.T.J.
Funding acquisition: C.F.Z., H.Z.
Investigation: S.A., C.F.Z., X.T.J.
Methodology: C.F.Z., J.S.Q., H.Z.
Project administration: C.F.Z.
Resources and Software: C.F.Z., H.Z., J.S.Q.
Supervision: C.F.Z.
Validation, Visualization: C.F.Z., H.Z., J.S.Q.
Writing: C.F.Z., S.A., X.T.J.
Review and editing: C.F.Z., J.S.Q.

Declaration of Competing Interest

The authors declare that they have no known competing financial interests or personal relationships that could have appeared to influence the work reported in this paper.

Acknowledgments

S.A. and X.J. contributed equally to this work. This project was supervised by C.F.Z. The manuscript was co-written by C.F.Z., S.A., X.J. and contributed by all co-authors. C.Z. and S.A. would like to thank the supports from Empa internal research grants (IRC 2019 and IRC 2020) as well as the ETH board (project FOXIP). X.J. acknowledges the support of the National Natural Science Foundation of China (Grant No. 61805146).

Conflict of interest

The authors declare no conflict of interest.

Data availability

The datasets generated during and/or analyzed during the current study are available from the corresponding author on reasonable request.

References

[1] A.K. Geim, K.S. Novoselov, Nat. Mater. 6 (2007) 183–191.
[2] K.S. Novoselov et al., Nature 438 (2005) 197–200.
[3] R.R. Nair et al., Science 320 (2008) 1308.
[4] K.R. Paton et al., Nat. Mater. 13 (2014) 624–630.
[5] H. Zhang, ACS Nano 9 (2015) 9451–9469.
[6] S. Abdolhosseinzadeh, H. Asgharzadeh, H.S. Kim, Sci. Rep. 5 (2015) 10160.
[7] Z. Zhang et al., Wiley Interdiscip. Rev. Comput. Mol. Sci. 6 (2016) 324–350.
[8] A.G. Kelly et al., Science 356 (2017) 69–73.
[9] M. Naguib, Y. Gogotsi, Acc. Chem. Res. 48 (2015) 128–135.
[10] S. Abdolhosseinzadeh, S. Sadighikia, S. Alkan Gürsel, ACS Sustain. Chem. Eng. 6 (2018) 3773–3782.
[11] A. Harvey et al., Chem. Mater. 27 (2015) 3483–3493.
[12] C.J. Zhang et al., Small 13 (2017) 1701677.
[13] E. Varrla et al., Chem. Mater. 27 (2015) 1129–1139.
[14] Z. Gholamvand et al., Chem. Mater. 28 (2016) 2641–2651.
[15] C.J. Zhang et al., J. Power Sources 274 (2015) 121–129.
[16] D. Zhang et al., J. Energy Chem. 27 (2018) 128–145.
[17] X. Xiao et al., Chem. Soc. Rev. 47 (2018) 8744–8765.
[18] A.J. Mannix et al., Science 350 (2015) 1513–1516.
[19] A. Iqbal et al., Science 369 (2020) 446–450.
[20] Y. Gogotsi, B. Anasori, ACS Nano 13 (2019) 8491–8494.
[21] J. Zhang et al., Adv. Mater. (2020) 2001093.
[22] V. Kamysbayev et al., Science 369 (2020) 979–983.
[23] S. Niu et al., ACS Nano 12 (2018) 3928–3937.
[24] X. Jiang et al., Phys. Rep. 848 (2020) 1–58.
[25] C.J. Zhang et al., Energy Environ. Mater. 3 (2020) 29–55.
[26] C.J. Zhang, V. Nicolosi, Energy Storage Mater. 16 (2019) 102–125.
[27] S. Abdolhosseinzadeh, J. Heier, C.J. Zhang, J. Phys. Energy 2 (2020) 31004.
[28] F. Shahzad et al., Science 353 (2016) 1137–1140.
[29] Z. Zeng et al., Adv. Sci. (2020) 2000979.
[30] C.J. Zhang et al., InfoMat 2 (2020) 613–638.
[31] Y. Lei et al., Small 15 (2019) 1901190.
[32] W. Ouyang et al., Adv. Electron. Mater. 6 (2020) 2000168.
[33] H. Fu et al., Adv. Energy Mater. 9 (2019) 1900180.
[34] M. Vural et al., Adv. Funct. Mater. 28 (2018) 1801972.
[35] C.J. Zhang et al., Nat. Commun. 10 (2019) 1795.
[36] S. Abdolhosseinzadeh et al., Adv. Mater. 32 (2020) 2000716.
[37] D. Xu et al., Adv. Funct. Mater. 30 (2020) 2000712.

[38] H. Kim, H.N. Alshareef, ACS Mater. Lett. 2 (2020) 55–70.
[39] K. Rasool et al., Mater. Today 30 (2019) 80–102.
[40] M. Naguib et al., ACS Nano 6 (2012) 1322–1331.
[41] J. Yang et al., J. Am. Ceram. Soc. 99 (2016) 660–666.
[42] G. Deysher et al., ACS Nano 14 (2019) 204–217.
[43] O. Mashtalir et al., Nat. Commun. 4 (2013) 1–7.
[44] M. Naguib et al., Adv. Mater. 23 (2011) 4248–4253.
[45] A. Gkountaras et al., Small 16 (2020) 1905784.
[46] A. Lipatov et al., Adv. Electron. Mater. 2 (2016) 1600255.
[47] M. Alhabeb et al., Chem. Mater. 29 (2017) 7633–7644.
[48] C. Zhang et al., Chem. Mater. 28 (2016) 3937–3943.
[49] M. Ghidiu et al., Chem. Commun. 50 (2014) 9517–9520.
[50] M. Seredych et al., Chem Mater 31 (2019) 3332.
[51] B. Anasori et al., ACS Nano 9 (2015) 9507–9516.
[52] Q. Tao et al., Nat. Commun. 8 (2017) 1–7.
[53] B. Ahmed, A. El Ghazaly, J. Rosen, Adv. Funct. Mater. (2020) 2000894.
[54] M. Ghidiu et al., Nature 516 (2014) 78–81.
[55] J. Halim et al., Adv. Funct. Mater. 26 (2016) 3118–3127.
[56] J. Zhou et al., Angew. Chem. - Int. Ed. 55 (2016) 5008–5013.
[57] J. Halim et al., Chem. Mater. 26 (2014) 2374–2381.
[58] X. Zhang, Z. Zhang, Z. Zhou, J. Energy Chem. 27 (2018) 73–85.
[59] T. Li et al., Angew. Chem. Int. Ed. Engl. 130 (2018) 6223–6227.
[60] E.H. Kisi et al., J. Phys. Chem. Solids 59 (1998) 1437–1443.
[61] J. Travaglini et al., Corros. Sci. 45 (2003) 1313–1327.
[62] M. Alhabeb et al., Angew. Chem. Int. Ed. 57 (2018) 5444–5448.
[63] P. Urbankowski et al., Nanoscale 8 (2016) 11385–11391.
[64] B. Soundiraraju, B.K. George, ACS Nano 11 (2017) 8892–8900.
[65] P. Urbankowski et al., Nanoscale 9 (2017) 17722–17730.
[66] Y. Li et al., Nat. Mater. 19 (2020).
[67] O. Mashtalir et al., Adv. Mater. 27 (2015) 3501–3506.
[68] M. Naguib et al., Dalt. Trans. 44 (2015) 9353–9358.
[69] G. Ying et al., FlatChem 8 (2018) 25–30.
[70] M.R. Lukatskaya et al., Science 341 (2013) 1502–1505.
[71] K. Huang et al., Chem. Soc. Rev. 47 (2018) 5109–5124.
[72] K. Hantanasirisakul, Y. Gogotsi, Adv. Mater. 30 (2018).
[73] J.L. Hart et al., Nat. Commun. 10 (2019) 522.
[74] Y. Lei et al., Ceram. Int. 45 (2019) 17653–17661.
[75] M. Mariano et al., Nanoscale 8 (2016) 16371–16378.
[76] C.J. Zhang et al., Adv. Mater. 29 (2017) 1702678.
[77] R. Sun et al., Adv. Funct. Mater. 27 (2017) 1702807.
[78] A.D. Dillon et al., Adv. Funct. Mater. 26 (2016) 4162–4168.
[79] H.A. Tahini, X. Tan, S.C. Smith, Nanoscale 9 (2017) 7016–7020.
[80] N.M. Caffrey, Nanoscale 10 (2018) 13520–13530.
[81] T. Schultz et al., Chem. Mater. 31 (2019) 6590–6597.
[82] Z. Wang, H. Kim, H.N. Alshareef, Adv. Mater. 30 (2018) 1706656.
[83] Y. Liu, H. Xiao, W.A. Goddard, J. Am. Chem. Soc. 138 (2016) 15853–15856.
[84] Z. Kang et al., Adv. Electron. Mater. 3 (2017) 1700165.
[85] J.K. El-Demellawi et al., ACS Nano 12 (2018) 8485–8493.
[86] K. Chaudhuri et al., ACS Photonics 5 (2018) 1115–1122.
[87] D. Huang et al., Adv. Mater. 31 (2019) 1901117.
[88] Q. Xue et al., Adv. Mater. 29 (2017) 1604847.
[89] X. Jiang et al., Laser Photonics Rev. 12 (2018) 1700229.
[90] G. Wang et al., Adv. Opt. Mater. (2020) 1902021.
[91] X. Jiang et al., Npj 2D Mater. Appl. 3 (2019) 1–9.
[92] Y. Dong et al., Adv. Mater. 30 (2018) 1705714.
[93] V. Mauchamp et al., Phys. Rev. B - Condens. Matter Mater. Phys. 89 (2014) 235428.
[94] Y. Zhang, F. Li, J. Magn. Magn. Mater. 433 (2017) 222–226.
[95] G. Gao et al., Nanoscale 8 (2016) 8986–8994.
[96] L. Hu, X. Wu, J. Yang, Nanoscale 8 (2016) 12939–12945.
[97] J. He, P. Lyu, P. Nachtigall, J. Mater. Chem. C 4 (2016) 11143–11149.
[98] Y. Yoon et al., Nanoscale 10 (2018) 22429–22438.
[102] Z. Ling et al., Proc. Natl. Acad. Sci. U. S. A. 111 (2014) 16676–16681.
[105] C.J. Zhang et al., Chem. Mater. 29 (2017) 4848–4856.
[106] X. Li et al., ACS Nano 14 (2020) 541–551.
[107] X. Li et al., Adv. Energy Mater. 10 (2020) 2001791.
[108] M. Naguib et al., Chem. Commun. 50 (2014) 7420–7423.
[109] Q. Yang et al., ACS Nano 13 (2019) 8275–8283.
[110] H. Pazniak et al., ACS Appl. Nano Mater. 3 (2020) 3195–3204.
[111] S. Huang, V.N. Mochalin, Inorg. Chem. 58 (2019) 1958–1966.
[112] J. Zhang et al., ACS Appl. Mater. Interfaces 12 (2020) 34032–34040.
[113] S. Huang, V. Mochalin, ACS Nano 14 (2020) 10251–10257.
[114] V. Natu et al., Angew. Chem. Int. Ed. 58 (2019) 12655–12660.
[115] T. Habib et al., Npj 2D Mater. Appl. 2 (2018) 20.
[116] X. Zhao et al., Matter 1 (2019) 513–526.
[117] K. Maleski, V.N. Mochalin, Y. Gogotsi, Chem. Mater. 29 (2017) 1632–1640.
[118] S. Seyedin et al., Glob. Challenges 3 (2019) 1900037.
[119] G. Hu et al., Chem. Soc. Rev. 47 (2018) 3265–3300.
[120] M.E. Schrader, Langmuir 11 (1995) 3585–3589.
[121] C. Battaglia et al., J. Phys. Condens. Matter 21 (2009) 013001.
[122] M. Grüßer et al., Langmuir 35 (2019) 12356–12365.
[123] A. Matavž, V. Bobnar, B. Malič, Langmuir 33 (2017) (1900) 11893–11901.
[124] D.K. Owens, R.C. Wendt, J. Appl. Polym. Sci. 13 (1969) 1741–1747.
[125] D.H. Kaelble, J. Adhes. 2 (1970) 66–81.
[126] A. Verma et al., Mater. Adv. 1 (2020) 153–160.
[127] G. Hu et al., Sci. Adv. 6 (2020) eaba5029.
[128] J.N. Coleman et al., Science 331 (2011) 568–571.
[129] D. Kim et al., ACS Nano 13 (2019) 13818–13828.
[130] R. Steller, J. Iwko, Polym. Eng. Sci. 58 (2018) 1446–1455.
[131] F. Galindo-Rosales, Appl. Sci. 6 (2016) 206.
[132] T.F. Tadros, Rheology of Dispersions, Wiley-VCH Verlag GmbH & Co. KGaA, Weinheim, Germany, 2010.
[133] L.W.T. Ng et al., Adv. Funct. Mater. 29 (2019) 1807933.
[134] T.G. Mezger, The Rheology Handbook, Vincentz Network, Hannover, Germany, 2019.
[135] A.P. Deshpande, J.M. Krishnan, P.B.S. Kumar, Rheology of Complex Fluids, Springer, New York, 2010.
[136] F. Cuomo, M. Cofelice, F. Lopez, Polymers 11 (2019) 259.
[137] B. Akuzum et al., ACS Nano 12 (2018) 2685–2694.
[138] W. Yang et al., Adv. Mater. 31 (2019) 1902725.
[139] K. Hantanasirisakul et al., Adv. Electron. Mater. 2 (2016) 1600050.
[140] S. Naficy et al., Mater. Horizons 1 (2014) 326–331.
[141] G. Ovarlez, Q. Barral, P. Coussot, Nat. Mater. 9 (2010) 115–119.
[142] M.R. Somalu et al., Renew. Sustain. Energy Rev. 75 (2017) 426–439.
[143] L.W.T. Ng et al., Graphene Relat. 2D Mater., Springer International Publishing, 2019, pp. 135–178.
[144] J. Dai et al., Chem. Soc. Rev. 49 (2020) 1756–1789.
[145] B. Derby, Annu. Rev. Mater. Res. 40 (2010) 395–414.
[146] G. Hu et al., Nat. Commun. 8 (2017) 278.
[147] L. Yu et al., Adv. Energy Mater. 9 (2019) 1901839.
[148] X. Li et al., Adv. Energy Mater. 10 (2020) 1903794.
[149] J. Orangi et al., ACS Nano 14 (2020) 640–650.
[150] W. Cao et al., Adv. Funct. Mater. 29 (2019) 1905898.
[151] P. Salles et al., Small 14 (2018) 1802864.
[152] H. An et al., Sci. Adv. 4 (2018) eaaq0118.
[153] T.H. Park et al., ACS Nano 13 (2019) 6835–6844.
[154] S. Uzun et al., Adv. Funct. Mater. 29 (2019) 1905015.
[155] P. Salles et al., Adv. Funct. Mater. 29 (2019) 1809223.
[156] Y. Zhang et al., Adv. Mater. 32 (2020) 1908486.
[157] Q. Jiang et al., Adv. Energy Mater. 9 (2019) 1901061.
[158] H. Huang et al., J. Power Sources 415 (2019) 1–7.
[159] X. Li et al., ChemElectroChem 7 (2020) 821–829.
[160] Y.-Y. Peng et al., Energy Environ. Sci. 9 (2016) 2847–2854.
[161] Y. Dong et al., Nano Energy 44 (2017) 103–110.
[162] M. Zhao et al., Adv. Mater. Technol. 4 (2019) 1800639.
[163] A. Sarycheva et al., Sci. Adv. 4 (2018) eaau0920.
[164] C.J. Zhang, V. Nicolosi, 2D Met. Carbides Nitrides Struct. Prop. Appl., Springer International Publishing, Carbides Nitrides Struct. Prop. Appl., 2019, pp. 481–501.
[165] L. Yang et al., J. Mater. Chem. A 7 (2019) 5635–5642.
[166] B. Xu et al., Adv. Mater. 28 (2016) 3333–3339.
[167] S. Ahn et al., Adv. Mater. 32 (2020) 2000919.
[168] H. Huang et al., Nano Energy 69 (2020) 104431.
[169] B. Lyu et al., ACS Nano 13 (2019) 11392–11400.
[170] K. Montazeri et al., Adv. Mater. 31 (2019) 1903271.
[171] J. Shen et al., Adv. Funct. Mater. (2018) 1801511.
[172] C.J. Zhang et al., Nat. Commun. 10 (2019) 849.
[173] N. Kurra et al., Adv. Energy Mater. 6 (2016) 1601372.
[174] Y. Wei et al., Electrochim. Acta 188 (2016) 385–392.
[175] J. Xiong et al., Electrochim. Acta 268 (2018) 503–511.
[176] F. Du et al., Electrochim. Acta 235 (2017) 690–699.
[177] C.J. Zhang et al., Adv. Funct. Mater. 26 (2016) 4143–4151.
[178] M. Naguib et al., Electrochem. Commun. 16 (2012) 61–64.
[179] H. Tang et al., Adv. Sci. 4 (2018) 1800502.
[180] X. Xie et al., Nano Energy 26 (2016) 513–523.
[181] X. Guo et al., Energy Storage Mater. 14 (2018) 306–313.

[182] D. Guo et al., Nano Energy 61 (2019) 478–485.
[183] J. Yan et al., Adv. Funct. Mater. 27 (2017) 1701264.
[184] R. Zhao et al., Energy Environ. Sci. 13 (2020) 246–257.
[185] J.J. Richardson et al., Chem. Rev. 116 (2016) 14828–14867.
[186] J. Lipton et al., Matter 2 (2020) 1148–1165.
[187] M.-Q. Zhao et al., Adv. Mater. 29 (2017) 1702410.
[188] J. Wang et al., Nat. Commun. 8 (2017) 1–9.
[189] J. Wang et al., Angew. Chem. Int. Ed. (2020). anie.202007063.
[190] S. Zhao et al., ACS Nano 12 (2018) 11193–11202.
[191] X. Guo et al., J. Mater. Chem. A (2014).
[192] L. Jiao et al., Adv. Energy Mater. 9 (2019) 1900219.
[193] Y.T. Liu et al., Adv. Mater. 30 (2018).
[194] D.I. Petukhov et al., Nanoscale 11 (2019) 9980–9986.
[195] J.D. Cain et al., ACS Nano 13 (2019) 12385–12392.
[196] T. Yun et al., Adv. Mater. 32 (2020) 1906769.
[197] S. Shi et al., Angew. Chem. Int. Ed. 58 (2019) 18171–18176.
[198] S.J. Kim et al., ACS Appl. Mater. Interfaces 11 (2019) 32320–32327.
[199] G. Eda, G. Fanchini, M. Chhowalla, Nat. Nanotechnol. 3 (2008) 270–274.
[200] H. Tang et al., Adv. Funct. Mater. 29 (2019) 1901907.
[201] J. Lao et al., ACS Nano 12 (2018) 12464–12471.
[202] M.R. Lukatskaya et al., Nat. Energy 2 (2017) 17105.
[203] J. Liu et al., Adv. Mater. 29 (2017) 1702367.
[204] M.-Q. Zhao et al., Adv. Mater. 27 (2015) 339–345.
[205] L. Ding et al., Angew. Chem. 129 (2017) 1851–1855.
[206] M.Q. Zhao et al., Nano Energy 30 (2016) 603–613.
[207] H.E. Karahan et al., Adv. Mater. 32 (2020) 1906697.
[208] C.J. Zhang et al., Adv. Funct. Mater. 28 (2018) 1705506.
[209] H. Hu, T. Hua, J. Mater. Chem. A 5 (2017) 19639–19648.
[210] E. Quain et al., Adv. Mater. Technol. 4 (2019) 1800256.
[211] E.A. Mayerberger et al., J. Appl. Polym. Sci. 134 (2017) 45295.
[212] C. Ji et al., ACS Appl. Mater. Interfaces 12 (2020) 24298–24307.
[213] P. Zhang et al., Adv. Funct. Mater. 30 (2020) 2000922.
[214] Y. Cai et al., ACS Nano 12 (2018) 56–62.
[215] Y. Yue et al., ACS Nano 12 (2018) 4224–4232.
[216] M. Aymerich et al., Materials 9 (2016) 728.
[217] H. Huang et al., ACS Nano 13 (2019) 3448–3456.